Timescale competition dictates thermo-mechanical responses of NiTi shape memory alloy bars

Zhuo, Mingzhao

DOI
10.1016/j.ijsolstr.2020.02.021

Publication date
2020

Document Version
Final published version

Published in
International Journal of Solids and Structures

International Journal of Solids and Structures 193–194 (2020) 601–617

Contents lists available at ScienceDirect

International Journal of Solids and Structures

journal homepage: www.elsevier.com/locate/ijsolstr

Timescale competition dictates thermo-mechanical responses of NiTi shape memory alloy bars

Mingzhao Zhuo[a,b,*]

[a] Department of Mechanical and Aerospace Engineering, The Hong Kong University of Science and Technology, Clear Water Bay, Hong Kong, China
[b] Faculty of Civil Engineering and Geosciences, Delft University of Technology, Delft, The Netherlands

ARTICLE INFO

Article history:
Received 9 September 2019
Revised 21 January 2020
Accepted 12 February 2020
Available online 17 February 2020

Keywords:
Thermo-mechanical coupling
Shape memory alloy
Phase transition
Thermodynamic driving force
Loading-rate effect
Timescale ratio

ABSTRACT

NiTi shape memory alloys (SMAs) exhibit distinct thermo-mechanical behaviors affected by the loading frequency, ambient conditions, and the specimen geometry. The effects of these factors are essentially due to the competition of different timescales in phase transitions of NiTi SMAs. However, quantifying the timescale competition still remains a challenge for SMAs subjected to force- or displacement-controlled cyclic loadings. Here we present a thermo-mechanically coupled model for one-dimensional SMA bars to address the effects of timescale competition on the thermo-mechanical responses. Scaling the model gives a dimensionless number λ indicating the ratio of the loading time to the characteristic time of heat transfer (affected by ambient conditions and the specimen geometry). The model shows that it is the timescale ratio λ that dictates the thermo-mechanical responses. Comparison of simulation results with experimental data validates the coupled model and the effects of the timescale ratio λ on the thermo-mechanical responses. The coupled model can predict the responses of SMAs under different combinations of external loadings and ambient conditions and thus provide guidelines for experimental design.

1. Introduction

Superelastic NiTi shape memory alloys (SMAs) have been widely used in practical applications from biomedical stents to vibration control devices (Lagoudas, 2008; Jani et al., 2014; Zhuo et al., 2019) and thereby attracted extensive research. The thermal and mechanical behaviors of SMAs are intrinsically coupled through phase transitions (Shaw, 2000; Yin et al., 2014; Morin et al., 2011b). In spite of broad constitutive models (Matsuzaki and Naito, 2004; Cisse et al., 2016) available for SMAs, modeling of the timescale competition during SMA phase transitions (He et al., 2010; He and Sun, 2011; Yin et al., 2013, 2014) still requires further improvement to consider general external loading modes. For insights into the timescale competition and its impact on SMA responses, we present a thermo-mechanically coupled model with explicit terms expressing the coupling between the two fields and the timescale competition, and the model is tailored specifically to a one-dimensional SMA bar under force- or displacement-controlled cyclic loadings.

The mechanical and thermal fields are fully coupled during phase transitions of NiTi SMAs. On the one hand, the stress-induced phase transitions cause temperature variation. Under external loadings, SMA phase transitions are accompanied by release (austenite to martensite A → M) and absorption (M → A) of latent heat (Auricchio and Sacco, 2001; Bernardini and Pence, 2002; Auricchio et al., 2008; Morin et al., 2011a; Yin et al., 2014). Apart from the latent heat, the intrinsic dissipation of mechanical energy, manifested as the stress strain hysteresis, is always converted into thermal energy as another heat source, which is about one order of magnitude smaller than the latent heat (Yin et al., 2014). The released/absorbed heat at the domain front of phase transitions will transfer via conduction within the specimen and through convection between the material and the ambient environment (Sun et al., 2012), thus leading to temperature variation in the specimen. On the other hand, the temperature change affects the stress strain responses of NiTi SMA bars. According to Clausius-Clapeyron relation (Yin et al., 2014), the transition stress is temperature-dependent: under isothermal conditions, the higher the ambient temperature, the higher the transition stress (Yin et al., 2013, 2014). It is remarked that for general thermo-elastic materials, the mechanical and thermal fields are actually slightly

* Corresponding author.
E-mail address: mzhuo@connect.ust.hk

https://doi.org/10.1016/j.ijsolstr.2020.02.021

coupled (Gough-Joule effect) (Schweizer and Wauer, 2001; Hetnarski and Eslami, 2009), but the coupling is negligible compared to that from phase transitions. The thermo-mechanical coupling accounts for experimental observations such as the strong dependence of thermo-mechanical responses on loading rates (Ortíin and Planes, 1989; Leo et al., 1993; Shaw and Kyriakides, 1995, 1997; Entemeyer et al., 2000; Lim and McDowell, 2002; Auricchio et al., 2008; He and Sun, 2010a, 2010b; Zhang et al., 2010; Sun et al., 2012; Morin et al., 2011a, 2011b; Grandi et al., 2012) (especially in cyclic loading and deformation (Yin et al., 2014)), on ambient conditions (Leo et al., 1993; Shaw and Kyriakides, 1995; Iadicola and Shaw, 2004; Shaw et al., 2008; Mirzaeifar et al., 2011; Grandi et al., 2012), and on the specimen geometry (Shaw et al., 2008; Mirzaeifar et al., 2011).

To understand these observed effects, different timescales in phase transitions need to be identified. For an SMA bar under tensile loading, two timescales exist in the mechanical field: one is the characteristic time for stress wave propagation in the specimen (Shaw et al., 2008); the other is the characteristic time of loading. Usually, the loading timescale is much longer than that of the stress wave propagation in tensile tests, rendering the bar in mechanical equilibrium at each time instant. This situation is called the quasi-static loading, under which the stress can be safely assumed uniform throughout the bar. Associated with the thermal field are the characteristic time of heat conduction within the specimen and the characteristic time of convective heat transfer. Thermal field is intrinsically heterogeneous due to formation and propagation of localized phase-transition domains (Shaw, 2000; Sun and Li, 2002; Feng and Sun, 2006; Churchill et al., 2009; He and Sun, 2010b; Zhang et al., 2010). Based on experimental observations (Yin et al., 2014), transition domains randomly form in the specimen and heat conduction is much faster than the heat release/absorption at domain fronts. Thus, we ignore the timescale of heat conduction and the spatial heterogeneity of temperature in the spirit of the lumped analysis (Cotta and Mikhailov, 1997; Yin et al., 2014). In conclusion, the two timescales of loading and convective heat transfer are of major importance, and their competition is responsible for the aforementioned effects.

A number of constitutive models (together with the heat equation and suitable numerical techniques) have been developed to describe the thermo-mechanical responses of SMAs. Liang and Rogers (1990) and Brinson (1993) developed a one-dimensional constitutive model to describe thermo-mechanical behavior of SMAs, reproducing pseudo-elastic and shape memory effects. Abeyaratne and Kim (1997) presented a one-dimensional model for SMAs under cyclic loadings. Bernardini and Pence (2002) derived models for macroscopic behavior of SMAs based on a free energy function and a dissipation function and presented thermodynamic driving forces to account for the hysteresis. Bernardini and Rega (2017) recently proposed a comprehensive thermomechanical modeling framework and compared the performances of various less-refined SMA models. In particular, the authors delivered a germane discussion on the thermomechanical coupling behavior. Auricchio and Sacco (2001) and Auricchio et al. (2008) established a uniaxial constitutive model based on Helmholtz free energy with an internal scalar variable—the martensite fraction; the model considered latent heat and mechanical dissipation simultaneously. Christ and Reese (2009) proposed a thermo-mechanically coupled SMA model in the framework of large strains, with the tension compression asymmetry considered. Morin et al. (2011a) modified the three-dimensional ZM model (Zaki and Moumni, 2007a, 2007b; Moumni et al., 2008) to take into account thermo-mechanical coupling, and then implemented the coupled ZM model into a finite element code for simulation of a superelastic SMA cylinder. The coupled model was also used to compare simulations with experimental results of SMA wires under cyclic loading (Morin et al., 2011b). Lagoudas and coworkers (Boyd and Lagoudas, 1996; Lagoudas et al., 2012) presented a three dimensional thermo-mechanical model that captured the smooth transition in the thermal and mechanical responses and added stress dependency to the concept of critical thermodynamic force. Grandi et al. (2012) proposed a one-dimensional Ginzburg–Landau model for the macroscopic behavior of SMAs. The influences of the strain rate and ambient conditions on the responses were highlighted. Yu et al. constructed a crystal plasticity based constitutive model (Yu et al., 2013) to describe the cyclic deformation of NiTi SMAs and then extended it to describe rate-dependent cyclic deformation (Yu et al., 2014) by considering the internal heat production and temperature evolution. Later on they proposed a 3D thermo-mechanical model (Yu et al., 2015) to consider dislocation slipping in austenite phase. Armattoe et al. (2016) proposed a coupled thermo-mechanical model for SMAs focusing on latent heat effects during forward and reverse phase transformations.

The above coupled models can be implemented to simulate the effects of the multiple factors: the loading rate, ambient conditions, and the specimen geometry (Morin et al., 2011a, 2011b; Grandi et al., 2012; Mirzaeifar et al., 2011). However, these effects were often studied individually. Typically, the thermo-mechanical responses (*e.g.*, stress strain curves, temperature evolution, and the hysteresis) were shown as functions of the applied strain rate with the heat transfer coefficient and specimen radius fixed at various values. For example, the non-monotonic strain-rate dependence curve of the hysteresis was shown to move towards higher strain rates when the heat transfer coefficient increases (Morin et al., 2011a; Grandi et al., 2012) but towards lower rates if the specimen radius increases (Morin et al., 2011a). These observations suggest the potential to incorporate the loading rate, ambient conditions, and the specimen geometry into a single parameter for better understanding of the governing mechanism.

Actually, recent experimental and modeling studies (He et al., 2010; He and Sun, 2011; Yin et al., 2013, 2014) have shown that the effects of these factors are attributed to the timescale competition during SMA phase transitions. He et al. (2010) and Yin et al. (2013) experimentally showed the non-monotonic dependence of the hysteresis on the timescale competition that reflects the strain rate and ambient conditions. He and Sun (2011) presented a model to explain and quantify the strain-rate dependence of the hysteresis: they solved the heat transfer equation and calculated the hysteresis from the temperature profile. Yin et al. (2014) reported systematic experimental results of the thermo-mechanical responses at a wide range of frequencies. These studies found that the frequency-dependent variations in temperature, stress, and hysteresis are determined by the competition between the time of the heat release/absorption (*i.e.*, the phase transition time) and the time of the heat transfer to the ambient. However, to connect the phase transition timescale to the external loading timescale, the modeling in these studies relies on the assumption that the latent heat release/absorption linearly depends on the applied strain rate. This assumption ignores the time for elastic deformation and thus is only suited to the displacement-controlled loading but not to the force-controlled case. Moreover, the evolution of the stress strain curve was not explicitly modeled and predicted.

The timescale competition is crucial to advancing our understanding of the resultant effect of the previously mentioned three factors, but it still remains a challenge to incorporate all the factors into the timescale competition by developing a coupled model that allows for general external loading modes and predicts both the mechanical and thermal responses. This study aims to quantify the timescale competition by presenting a one-dimensional model (Section 2) with clearly-formulated coupling terms, followed by scaling of the thermo-mechanically coupled

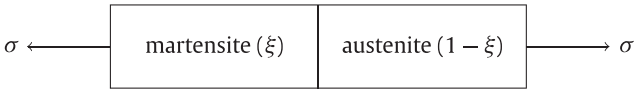

Fig. 1. Series model of a one-dimensional SMA bar under tensile loading. Here ξ represents martensite volume fraction.

model (Section 3.1). Built on many of the ideas in the previously cited literature, the one-dimensional model consists of the stress strain relation (Section 2.2), the heat equation (Section 2.5), and evolution rules (Section 2.4) to describe the progress of phase transitions. Scaling the governing equations permits us to derive a dimensionless number—the two-timescale ratio λ (Section 3.1). Then we study the effects of λ on the thermal and mechanical responses, in particular the damping capacity (Section 3.2). For the purpose of validation, we compare the model predictions with experimental results (Section 4). The numerical procedures (return mapping algorithm (Simo and Hughes, 1998)) for solving the governing equations are outlined in Appendix C.

2. Thermo-mechanically coupled model

Here we consider a one-dimensional bar under quasi-static tensile loading. Under this setting we assume uniform axial stress σ in the bar. With the lumped analysis (Cotta and Mikhailov., 1997; Yin et al., 2014), we further assume a uniform thermal field and use the average temperature T to describe the whole bar. Specific Gibbs free energy of an SMA bar (Section 2.1) is calculated by the rule of mixtures with martensite volume fraction as the internal variable; the stress strain relation (Section 2.2) and heat equation (Section 2.5) are thus derived according to the first and second laws of thermodynamics (Appendix A). To model the stress strain hysteresis, we assume positive and negative thermodynamic driving forces (Section 2.3) in the forward and reverse phase transitions, respectively; the relation between the thermodynamic driving force and martensite volume fraction (Section 2.4) is proposed on an empirical basis. Finally, prescribed strain or stress (Section 2.6) is also included to complete the coupled model.

2.1. Gibbs free energy of an SMA bar

For a linear elastic bar, the specific Gibbs free energy is readily available in references (Hetnarski and Eslami, 2009) and expressed here as

$$g = -\frac{\sigma^2}{2E} - \alpha(T - T_0)\sigma + c_\sigma\left(T - T_0 - T\ln\frac{T}{T_0}\right) + u_0 - Ts_0, \tag{1}$$

where E is the Young's modulus, α is the thermal expansion coefficient, c_σ is the specific heat capacity (per unit volume) at a constant stress, and u_0 and s_0 are the initial internal energy and entropy, respectively, per unit volume at reference temperature T_0 in the stress-free state. Here the stress σ refers to the axial stress as a scalar, not a tensor in the three-dimensional setting.

Now we extend the free energy expression to an NiTi SMA bar. Without loss of generality, the SMA bar consists of martensite with volume fraction ξ and austenite with volume fraction $(1-\xi)$. Here ξ takes value from 0 to 1: $\xi = 0$ and $\xi = 1$ correspond to pure austenite and pure martensite, respectively; otherwise, the bar is a mixture of austenite and martensite. Since the axial stress is uniform throughout the bar, we use a series model (Reuss bound, Fig. 1) to describe the bar composition, following Brinson and Huang (1996) and Auricchio and Sacco (1997).

In the series model, austenite is linear elastic, and its Gibbs free energy is expressed as

$$g_{\mathrm{A}} = -\frac{\sigma^2}{2E_{\mathrm{A}}} - \alpha_{\mathrm{A}}(T - T_0)\sigma + c^{\mathrm{A}}_\sigma\left(T - T_0 - T\ln\frac{T}{T_0}\right) + u_{0\mathrm{A}} - Ts_{0\mathrm{A}}. \tag{2}$$

However, martensite should be split into a linear elastic part and a transformed part that accounts for the transformation strain. The work done on the transformation strain is not dissipated but stored as potential energy in the transformed part of martensite. It will be released after the completion of the reverse phase transition from martensite to austenite. Gibbs free energy of martensite per unit volume is then given by

$$g_{\mathrm{M}} = -\frac{\sigma^2}{2E_{\mathrm{M}}} - \alpha_{\mathrm{M}}(T - T_0)\sigma + c^{\mathrm{M}}_\sigma\left(T - T_0 - T\ln\frac{T}{T_0}\right) + u_{0\mathrm{M}} - Ts_{0\mathrm{M}} - \epsilon_{\mathrm{L}}\sigma, \tag{3}$$

where the extra term $-\epsilon_{\mathrm{L}}\sigma$ represents the stored potential energy due to the transformation strain.

Thus, the specific Gibbs free energy of the SMA bar can be calculated by the rule of mixtures:

$$\begin{aligned} g_{\mathrm{mix}} &= \xi g_{\mathrm{M}} + (1-\xi)g_{\mathrm{A}} \\ &= -\frac{\sigma^2}{2E(\xi)} - \alpha(T - T_0)\sigma - \xi\epsilon_{\mathrm{L}}\sigma + c_\sigma\left(T - T_0 - T\ln\frac{T}{T_0}\right) \\ &\quad + u_0(\xi) - Ts_0(\xi), \end{aligned} \tag{4}$$

where

$$E(\xi) = [\xi/E_{\mathrm{M}} + (1-\xi)/E_{\mathrm{A}}]^{-1}, \tag{5}$$

$$u_0(\xi) = \xi u_{0\mathrm{M}} + (1-\xi)u_{0\mathrm{A}}, \tag{6}$$

$$s_0(\xi) = \xi s_{0\mathrm{M}} + (1-\xi)s_{0\mathrm{A}}. \tag{7}$$

In Eq. (4), we neglect the small difference in thermal expansion coefficient α and specific heat capacity c_σ between martensite and austenite and assume they are the same for both phases (Lagoudas, 2008; Morin et al., 2011a).

2.2. Constitutive relations

Substituting Gibbs free energy of the SMA bar Eq. (4) into Eq. (A.11), we obtain the following constitutive equations

$$\epsilon = \frac{\sigma}{E(\xi)} + \xi\epsilon_{\mathrm{L}} + \alpha(T - T_0), \tag{8}$$

$$s = \alpha\sigma + c_\sigma\ln\frac{T}{T_0} + s_0(\xi), \tag{9}$$

where $E(\xi)$ and $s_0(\xi)$ are defined in Eqs. (5) and (7), respectively. Unlike that stress σ and temperature T are assumed uniform, strain ϵ in Eq. (8) and entropy s in Eq. (9) are volume-averaged values of the whole bar.

2.3. Thermodynamic driving force

In view of Eq. (A.11), the Clausius-Planck inequality (A.10) will be reduced to

$$D_{\mathrm{m}} = -\frac{\partial g}{\partial \boldsymbol{\zeta}} : \dot{\boldsymbol{\zeta}} \geq 0. \tag{10}$$

For the SMA bar, martensite volume fraction ξ can be considered as the internal variable (Auricchio and Sacco, 2001; Zaki and Moumni, 2007b; Lagoudas et al., 2012) to replace $\boldsymbol{\zeta}$. In Eq. (10), we can define the energy derivative term as the thermodynamic driving force Π for the forward phase transition (A $\rightarrow$ M), conjugate to the internal variable ξ in the similar way as Eq. (A.11):

$$\Pi = -\frac{\partial g_{\mathrm{mix}}}{\partial \xi} = g_{\mathrm{A}} - g_{\mathrm{M}}. \tag{11}$$

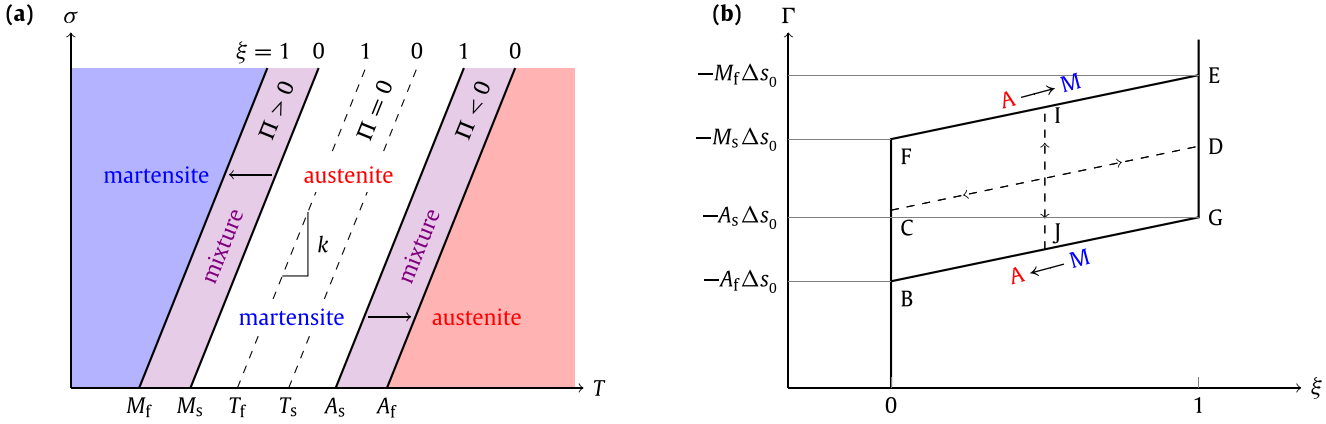

Fig. 2. Stress-temperature (σ-T) phase diagram (a) and control driving force Γ *versus* martensite volume fraction ξ (b). In panel (a), M_s and M_f are martensite start and finish temperatures for A → M phase transition, while A_s and A_f are austenite start and finish temperatures for M → A phase transition. In panel (b), $\Gamma = -T_s\Delta s_0$ at point C and $\Gamma = -T_f\Delta s_0$ at point D. IJ represents the loading/unloading path in the case of incomplete phase transitions (Appendix B). (For interpretation of the references to color in this figure, the reader is referred to the web version of this article.)

Thus, the physical meaning of the thermodynamic driving force is the Gibbs free energy difference between the two phases. To calculate the Gibbs free energy difference (11), we subtract Eq. (3) from Eq. (2) and obtain

$$\Pi(\sigma, T) = \sigma\epsilon_L - T\Delta s_0 + \Delta u_0, \tag{12}$$

where $\Delta s_0 = s_{0A} - s_{0M}$ and $\Delta u_0 = u_{0A} - u_{0M}$. Here we ignore the small elastic strain energy difference between the two phases so that they can cancel out each other.

Substituting the thermodynamic driving force Π into Eq. (10), we obtain a more concise form of the Clausius-Planck inequality:

$$D = \Pi\dot{\xi} \geq 0. \tag{13}$$

The non-negative dissipation restriction (13) indicates that positive thermodynamic driving force ($\Pi > 0$, $g_A > g_M$) corresponds to the forward phase transition (A → M, $\dot{\xi} \geq 0$), while negative thermodynamic driving force ($\Pi < 0$, $g_A < g_M$) leads to the reverse phase transition (M → A, $\dot{\xi} \leq 0$). If the thermodynamic driving force is zero ($\Pi = 0$, $g_A = g_M$), the two phases are in equilibrium and $\dot{\xi}$ can be either positive, negative or zero.

2.4. Evolution rules

As Eq. (12) shows, the thermodynamic driving force Π for phase transitions is a combination of stress and temperature; this agrees with the fact that phase transitions are driven by stress and/or temperature. However, we have not established any relation between thermodynamic driving force and martensite volume fraction. To this end, we introduce an additional interaction energy term expressed by

$$E_{\text{inter}} = -\Lambda\xi(1-\xi), \tag{14}$$

where Λ is a positive material constant ensuring negative interaction energy. This energy form follows the choice in Bernardini and Pence (2002) and is chosen because it is the simplest one that satisfies the intrinsic requirement of interaction energy: it should be zero for pure martensite ($\xi = 1$) and for pure austenite ($\xi = 0$).

The total Gibbs free energy is thus modified to

$$g_{\text{mix}} = -\frac{\sigma^2}{2E(\xi)} - \alpha(T - T_0)\sigma - \xi\epsilon_L\sigma + c_\sigma\left(T - T_0 - T\ln\frac{T}{T_0}\right) + u_0(\xi) - Ts_0(\xi) - \Lambda\xi(1-\xi), \tag{15}$$

and the thermodynamic driving force is changed to

$$\Pi(\sigma, T) = \Gamma + \Delta u_0 - \Lambda(2\xi - 1), \tag{16}$$

where Γ is defined as the control driving force (Bernardini and Pence, 2002)

$$\Gamma = \sigma\epsilon_L - T\Delta s_0, \tag{17}$$

as a linear combination of the two state variables σ and T.

At equilibrium, the minimization of the total Gibbs free energy g_{mix} requires the thermodynamic driving force to be zero ($\Pi = 0$), which gives the relation (evolution rule) between martensite volume fraction and control driving force:

$$\xi = \frac{\Gamma + \Delta u_0 + \Lambda}{2\Lambda}. \tag{18}$$

The null thermodynamic driving force, or Eq. (18), corresponds to a transition band zone delimited by two dashed boundary lines in the $\sigma - T$ phase diagram (Fig. 2a). In the stress-free state, the forward phase transition starts at T_s with $\xi = 0$ and ends at T_f with $\xi = 1$. Substituting these two conditions into Eq. (18) gives

$$\Delta u_0 = \frac{T_s + T_f}{2}\Delta s_0 \quad \text{and} \quad \Lambda = \frac{T_s - T_f}{2}\Delta s_0. \tag{19}$$

Thus, the evolution rule (18) changes to

$$\xi = \frac{\Gamma(\sigma, T) + T_s\Delta s_0}{(T_s - T_f)\Delta s_0}, \tag{20}$$

which exactly represents line CD in Fig. 2b.

The phase transition line CD (or $\Pi = 0$ in essence) represents a reversible loading-unloading path and no hysteresis is formed during the loading-unloading cycle. The null energy dissipation is however in contrast to the experimental observation of a hysteresis loop in the stress strain curve during phase transitions. Due to the frictional forces resisting the motion of interfaces and energy barrier between the two phases, extra energy is always needed to overcome these obstacles and to proceed the phase transition.

To model the hysteresis, we choose a positive thermodynamic driving force for the forward phase transition and a negative force for the reverse phase transition, in accordance with the non-negative dissipation restriction (13). Hence, in Fig. 2a, the transition band delimited by the two dashed lines is split into two band zones: the left-hand one with $\Pi > 0$ is for A → M phase transition and the other with $\Pi < 0$ for M → A phase transition. In the case of null stress, A → M phase transition starts at martensite start temperature M_s and ends at martensite finish temperature M_f, while M → A phase transition starts at austenite start temperature A_s and ends at austenite finish temperature A_f (Brinson, 1993; Brinson and Huang, 1996; Auricchio et al., 2008).

Accordingly in Fig. 2b, the reversible loading-unloading path CD is split into the forward loading path and the reverse unloading

Table 1
Governing equations for an SMA bar under prescribed loadings.

1. prescribed stress or strain:[a]	$\sigma = \frac{\sigma_{\max}}{2}(1-\cos\omega t)$ or $\epsilon = \frac{\epsilon_{\max}}{2}(1-\cos\omega t)$;	(30)
2. stress strain equation:	$\epsilon = \frac{\sigma}{E(\xi)} + \xi\epsilon_{\mathrm{L}} + \alpha(T-T_0)$;	(8)
3. heat equation:[b]	$c_\sigma \dot{T} = -T\alpha\dot{\sigma} + T\Delta s_0\dot{\xi} + \Pi\dot{\xi} - h\gamma(T-T_0)$;	(29)
4. evolution rules:	$\xi_{\mathrm{FT}} = \frac{\sigma\epsilon_{\mathrm{L}} - T\Delta s_0 + M_{\mathrm{s}}\Delta s_0}{(M_{\mathrm{s}}-M_{\mathrm{f}})\Delta s_0}$, $\xi_{\mathrm{RT}} = \frac{\sigma\epsilon_{\mathrm{L}} - T\Delta s_0 + A_{\mathrm{f}}\Delta s_0}{(A_{\mathrm{f}}-A_{\mathrm{s}})\Delta s_0}$.	(21)

[a] The loading can be applied in other format (*i.e.*, the triangular function with a constant loading rate).
[b] Π is given in Eq. (16) and constants therein are given by Eq. (24).

path. The two linear loading and unloading paths indicate linear relations between the control driving force Γ and martensite fraction ξ. Specifically, analogous to Eq. (20), the evolution rule for the forward phase transition is

$$\xi_{\mathrm{FT}} = \frac{\Gamma(\sigma,T) + M_{\mathrm{s}}\Delta s_0}{(M_{\mathrm{s}}-M_{\mathrm{f}})\Delta s_0}, \tag{21a}$$

and that for the reverse transition is

$$\xi_{\mathrm{RT}} = \frac{\Gamma(\sigma,T) + A_{\mathrm{f}}\Delta s_0}{(A_{\mathrm{f}}-A_{\mathrm{s}})\Delta s_0}, \tag{21b}$$

where $\Gamma = \sigma\epsilon_{\mathrm{L}} - T\Delta s_0$ is restricted to $-M_{\mathrm{s}}\Delta s_0 < \Gamma < -M_{\mathrm{f}}\Delta s_0$ in Eq. (21a) and to $-A_{\mathrm{f}}\Delta s_0 < \Gamma < -A_{\mathrm{s}}\Delta s_0$ in Eq. (21b).

Now we have four material parameters to determine: ϵ_{L}, Δs_0, Δu_0 and Λ. The transformation strain ϵ_{L} can be directly measured from experiments, while Δs_0 is calculated through the slope k of the straight lines (representing constant Γ values) in the $\sigma - T$ phase diagram (Fig. 2a). The slope k is the coefficient in Clausius-Clapeyron relation and can be obtained from experiments (Yin et al., 2014). Thus Δs_0 is calculated as

$$\Delta s_0 = k\epsilon_{\mathrm{L}}. \tag{22}$$

To determine constants Δu_0 and Λ, we assume equal dissipated energy in the forward and reverse phase transitions. This assumption suggests that in Fig. 2b, the reversible loading-unloading path CD cut the hysteresis loop BGEF in half, namely that C is the middle point of BF and D is the middle point of GE. Therefore, the transformation temperatures associated with C and D are expressed as

$$T_{\mathrm{s}} = \frac{M_{\mathrm{s}}+A_{\mathrm{f}}}{2} \quad \text{and} \quad T_{\mathrm{f}} = \frac{M_{\mathrm{f}}+A_{\mathrm{s}}}{2}, \tag{23}$$

respectively. According to Eq. (19), we obtain

$$\Delta u_0 = \frac{M_{\mathrm{s}}+M_{\mathrm{f}}+A_{\mathrm{s}}+A_{\mathrm{f}}}{4}\Delta s_0, \tag{24a}$$

$$\Lambda = \frac{M_{\mathrm{s}}-M_{\mathrm{f}}+A_{\mathrm{f}}-A_{\mathrm{s}}}{4}\Delta s_0. \tag{24b}$$

The four transformation temperatures (M_{s}, M_{f}, A_{s}, and A_{f}) in the stress-free state can be measured from experiments. Considering that phase transitions are determined by the control driving force Γ (linear combination of σ and T, Eq. (17) and Fig. 2a), we can also interpolate them from the four transformation stresses (σ_{Ms}, σ_{Mf}, σ_{As}, and σ_{Af}) at a given temperature (*e.g.*, the four transformation stresses at room temperature from the isothermal test in Fig. 6).

2.5. Heat equation

Substituting Eq. (13) into Eq. (A.4), we relate the thermodynamic driving force to the entropy change rate:

$$\Pi\dot{\xi} = T\dot{s} + \nabla\cdot\mathbf{q} - r. \tag{25}$$

This equation holds for every point in the domain considered, and the local heat flux divergence term $\nabla\cdot\mathbf{q}$ represents the outflow of heat through the boundaries of a particle. Since the lumped analysis (Cotta and Mikhailov., 1997) is adopted, we consider the SMA bar as a whole and use the volume-averaged heat outflow to replace the local term. To this end, we apply the volume average to $\nabla\cdot\mathbf{q}$ and use Gauss theorem to arrive at

$$\frac{1}{V}\int_\Omega \nabla\cdot\mathbf{q}\,\mathrm{d}V = \frac{1}{V}\int_{\partial\Omega}\mathbf{q}\cdot\mathbf{n}\,\mathrm{d}S = \frac{1}{V}hA(T-T_0) = h\gamma(T-T_0), \tag{26}$$

where h is the average coefficient of convective heat transfer, $\gamma = A/V$ is the surface area (A) to volume (V) ratio, and T_0 is the ambient temperature. The volume average of $\nabla\cdot\mathbf{q}$ represents the heat outflow from the SMA bar to the ambient environment. Since the bar has no internal heat source, the heat source term r can be discarded. Now we can rewrite Eq. (25) as

$$T\dot{s} = \Pi\dot{\xi} - h\gamma(T-T_0). \tag{27}$$

Taking the time derivative of the constitutive relation for entropy (Eq. (9)) and multiplying both sides by T, we have

$$T\dot{s} = T\alpha\dot{\sigma} + c_\sigma\dot{T} - T\Delta s_0\dot{\xi}. \tag{28}$$

Letting the right-hand sides of Eqs. (27) and (28) be equal gives the heat equation:

$$c_\sigma\dot{T} = -T\alpha\dot{\sigma} + T\Delta s_0\dot{\xi} + \Pi\dot{\xi} - h\gamma(T-T_0). \tag{29}$$

The physical meaning of each term in heat equation (29) is as follows:

1. $c_\sigma\dot{T}$ represents the thermal energy change rate;
2. $-T\alpha\dot{\sigma}$ represents the stress effect on temperature (thermoelastic effect) (Schweizer and Wauer, 2001);
3. $T\Delta s_0\dot{\xi}$ denotes the latent heat caused by entropy difference;
4. $\Pi\dot{\xi}$ denotes the dissipated mechanical energy manifested by the hysteresis loop;
5. $h\gamma(T-T_0)$ represents the heat outflow to the surroundings.

As shown in Eq. (29), the latent heat is released ($T\Delta s_0\dot{\xi} > 0$) in the forward phase transition and absorbed ($T\Delta s_0\dot{\xi} < 0$) in the reverse transition, while the hysteresis heat is always released ($\Pi\dot{\xi} > 0$).

2.6. Prescribed loading

So far we have derived three equations: the stress strain equation (8), heat equation (29), and evolution rules (21). The model is however not completed yet. In experiments, either the axial force or end displacement will be prescribed; accordingly, we can specify the stress as

$$\sigma(t) = \frac{\sigma_{\max}}{2}(1-\cos\omega t) \tag{30a}$$

or the strain as

$$\epsilon(t) = \frac{\epsilon_{\max}}{2}(1 - \cos\omega t), \tag{30b}$$

where ω is the angular frequency, and $\sigma_{\max}$ and $\epsilon_{\max}$ are the maximum stress and strain applied, respectively. It is remarked that we do not solve the equation of equilibrium since it is naturally satisfied under the assumption of uniform stress. In the displacement-controlled case, the end displacement is used to calculate the average strain of the whole bar.

3. Results and discussion

We first summarize all the governing equations in Table 1 for easier reference in the following discussions. In the coupled model, there are two types of coupling between the mechanical and thermal fields. The first type is the general thermo-elastic effect (Schweizer and Wauer, 2001) that is manifested by the thermal expansion term $\alpha(T - T_0)$ in Eq. (8) and the stress rate term $-T\alpha\dot{\sigma}$ in Eq. (29). The second type is caused by phase transitions: the transformation strain term $\xi\epsilon_L$ in Eq. (8) and the latent heat term $T\Delta s_0\dot{\xi}$ (plus the dissipation term $\Pi\dot{\xi}$) in Eq. (29) show that the two fields are coupled through the progress of phase transitions. The strong thermo-mechanical coupling phenomena observed in SMAs (Yin et al., 2013, 2014) is mainly caused by phase transitions, while the general thermo-elastic effect is relatively negligible (Schweizer and Wauer, 2001).

In the thermo-mechanical model, each field involves a timescale. Because of the coupling, the competition between the two timescales results in distinct responses. By scaling the governing equations we can derive a dimensionless number—the two-timescale ratio (Section 3.1). The effects of the timescale ratio on thermo-mechanical responses (Section 3.2) and hysteresis loop area (Section 3.2.2) are then studied.

3.1. Timescale analysis

The timescales of mechanical and thermal fields are manifested in Eqs. (30) and (29), respectively. We denote the loading time, half of a loading-unloading period, as $t_d = \pi/\omega$ and regard it as the characteristic timescale of mechanical loading. For triangular loading functions, the characteristic timescale t_d is simply the time to reach the maximum stress/strain. Letting $\tau = t/t_d$ in the prescribed stress/strain (Eq. (30)), we obtain

$$\sigma = \frac{\sigma_{\max}}{2}(1 - \cos\pi\tau), \tag{31a}$$

$$\epsilon = \frac{\epsilon_{\max}}{2}(1 - \cos\pi\tau). \tag{31b}$$

Replacing t with $t_d\tau$ in heat equation (29) gives

$$\dot{T} = -\frac{\alpha}{c_\sigma}T\dot{\sigma} + \frac{\sigma\epsilon_L + \Delta u_0 - \Lambda(2\xi - 1)}{c_\sigma}\dot{\xi} - \lambda(T - T_0), \tag{32}$$

where the overdot denotes the derivative with respect to τ, Δu_0 and Λ are given in Eq. (24), and λ is expressed as

$$\lambda = \frac{t_d}{c_\sigma/(h\gamma)}.$$

To see the physical meaning of the denominator term, we just keep the heat transfer term $-h\gamma(T - T_0)$ in the right-hand side of Eq. (29) and discard other terms. Thus the solution of Eq. (29) has the form of

$$T = T_0 + T_1 e^{-t/t_h}, \tag{33}$$

where T_1 is a constant depending on the initial condition, and t_h is expressed as

$$t_h = \frac{c_\sigma}{h\gamma}. \tag{34}$$

Therefore, t_h represents the characteristic time of convective heat transfer. The physical meaning of λ is hence the ratio of the loading time to the characteristic time of heat transfer:

$$\lambda = \frac{t_d}{t_h}. \tag{35}$$

Specifically, for an SMA bar of radius R, the surface area to volume ratio is $\gamma = 2/R$. Here the surface area specifically refers to the side area; the two ends are in contact with the clamps and the conduction between them is incorporated into the lumped heat transfer (Yin et al., 2014). Thus, the characteristic heat transfer time is reduced to the one reported in references (Bruno et al., 1995; He and Sun, 2011; Yin et al., 2014): $t_h = c_\sigma R/(2h)$.

In Eq. (32), a null λ means no heat exchange with the ambient environment and hence corresponds to the adiabatic condition; contrarily; an infinite λ corresponds to strong heat exchange and thus represents the isothermal condition. Note that, in the nondimensionalized governing equations, the timescale ratio λ is the only manipulated factor that can be changed to significantly impact the thermo-mechanical responses.

Eq. (35) shows that multiple factors affect the dimensionless number λ. Varying the loading frequency ω changes the loading timescale, while varying the surface area to volume ratio γ and the convective heat transfer coefficient h changes the heat transfer timescale. We thus have the following remarks.

1. When γ and h are fixed, $\omega \to 0$ results in the isothermal condition, while $\omega \to \infty$ leads to the adiabatic condition. The different responses due to varying ω is called the loading rate effect.
2. When γ and ω are fixed, $h \to 0$ gives the adiabatic condition, while $h \to \infty$ leads to the isothermal condition. Changing h leads to the effect of ambient conditions.
3. When h and ω are fixed, changing γ also impacts the thermo-mechanical responses, which is called the effect of surface area to volume ratio (determined by geometrical shape and size).

We can see that the loading rate effect, the effect of ambient conditions, and the effect of surface area to volume ratio are all due to the two-timescale competition through the thermo-mechanical coupling.

If h is held close to 0 or ∞, varying ω has no effect on the thermo-mechanical responses, *i.e.*, no rate effect. This is also remarked by Ivshin and Pence (1994) based on their model. Under isothermal condition ($h \to \infty$), no strain rate effect was observed in experiments by Grabe and Bruhns (2008). Nevertheless, the rate-independent responses under nearly adiabatic condition ($h \to 0$), as predicted by our model, still need further experimental validation.

3.2. Effects of the timescale ratio

The single parameter λ reflects the resultant effect of the three impacting factors—the loading rate, the ambient conditions, and the surface area to volume ratio. Thus it is possible to exhaust the thermo-mechanical responses under various conditions by studying the timescale ratio effect. To this end, we simulate the stress strain curves and temperature variation at different λ values to consider scenarios ranging from the adiabatic to the isothermal conditions. We consider two types of loading: stress-controlled (Eq. (31a)) and strain-controlled (Eq. (31b)). Material parameters are from Tables 2 and 3 and they are calibrated with experiments in Section 4.1. The ambient temperature T_0 is kept constant at room temperature 25 °C.

3.2.1. On thermo-mechanical responses

Fig. 3 shows results under the strain-controlled loading. Three typical λ values—1000, 3.2, and 0.01—are chosen to show responses under the isothermal condition, an intermediate heat transfer condition, and the adiabatic condition, respectively. In particular, the three λ values correspond to the three solid points A, B, and C in Fig. 5a. The isothermal case is realized by a large λ value (1000) that suggests very strong heat exchange with the ambient environment and thus leads to negligible temperature variation. The bar temperature almost remains constant at the room temperature as shown by the yellow line in Fig. 3b. According to Clausius-Clapeyron relation (Yin et al., 2014), no temperature change, no change in the phase transition stress. Therefore, a stress plateau is observed in the stress strain curve (yellow line in Fig. 3a). To be precise, in the phase transition processes a small stress change occurs due to the assumption of the phase transition band (Fig. 2a), which indicates different start and finish stresses of phase transitions at the same temperature. The isothermal condition can be achieved in experiments by very slow loading and fast flowing air around the specimen (He et al., 2010; Yin et al., 2014).

The adiabatic condition is approximately achieved by a small λ value (0.01), suggesting a negligible heat exchange with the surroundings. When the heat exchange is disregarded, the temperature will change in accordance with the latent heat release and absorption, as well as the hysteresis heat accumulation (Fig. 3b). As the forward phase transition starts, the temperature also starts to increase (latent heat release) until the end of the transition (II), and then it keeps constant during the unloading process of martensite (III). During the reverse transition (IV), the temperature keeps decreasing (latent heat absorption) and then levels off (V). At the end of unloading, the latent heat absorption cancels out its release and the accumulated hysteresis heat results in a small temperature rise, which is about 5% of the temperature increase in phase II caused by the latent heat release. This percentage agrees with the direct experimental measurement: the volumetric latent heat $l_0 = 7.74 \times 10^7$ J/m^3 is about 20 times larger than the steady-state hysteresis $D_s = 3.61 \times 10^6$ J/m^3 in Yin et al. (2014). In parallel with the temperature change, the transition stress increases steeply above the stress plateau in the forward phase transition, followed by a parallel stress decrease during the reverse transition. The stress at the end of the reverse transition is slightly higher than the isothermal transition stress due to the corresponding slight temperature rise. The hysteresis loop is thus slightly smaller than the isothermal one. It is remarked that we observe a small temperature drop—caused by the thermo-elastic effect—at the end of the loading of austenite (I). Nevertheless, the temperature drop is so small that the thermo-elastic effect is negligible compared to the phase transition effect.

When the latent heat release/absorption and heat exchange with the surroundings are comparable ($\lambda = 3.2$), the thermo-mechanical responses differ in the following aspects. First, the temperature increases moderately and starts to decreases in the middle of the forward phase transition (the peak in phase II). As temperature increases, the larger temperature difference $T - T_0$ enhances the heat exchange to the extent that the heat outflow outweighs the latent heat release. Second, in the reverse transition (IV), the temperature plummets and is driven below the room temperature, which is due to the fact that the heat released in

Table 2
Calibrated model parameters for displacement-controlled (cyclic) loading.

Parameter	symbol	value	unit
Young's modulus of austenite	E_A	25	GPa
Young's modulus of martensite	E_M	19.4	GPa
temperature dependence of transition stress	k	6.8	MPa/K
transformation strain	ϵ_L	0.043	-
specific heat capacity	c_σ	3.2×10^6	J/(m^{3}K)
thermal expansion coefficient	α	11×10^6	1/K
austenite → martensite start temperature	M_s	262.5	K
austenite → martensite finish temperature	M_f	261.0	K
martensite → austenite start temperature	A_s	281.0	K
martensite → austenite finish temperature	A_f	283.0	K

Table 3
Calibrated model parameters for force-controlled (cyclic) loading. Other model parameters not listed here take the same values as in Table 2.

Parameter	symbol	value	unit
transformation strain	ϵ_L	0.04	-
austenite → martensite start temperature	M_s	259.5	K
austenite → martensite finish temperature	M_f	258.0	K
martensite → austenite start temperature	A_s	273.0	K
martensite → austenite finish temperature	A_f	276.0	K

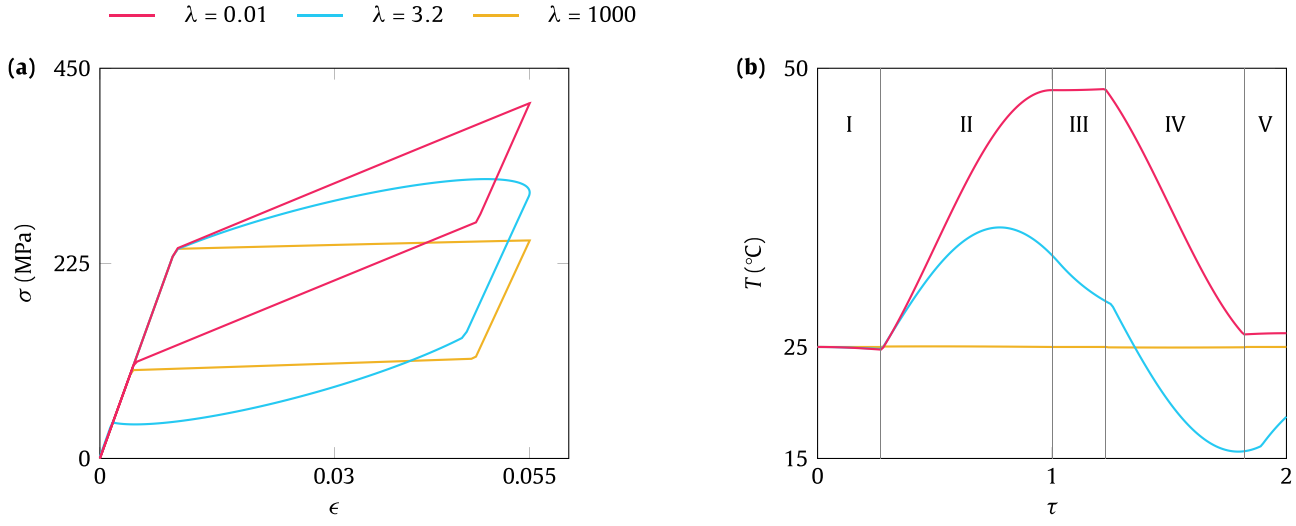

Fig. 3. Effects of the timescale ratio λ on the stress-strain (σ-ϵ) curve (a) and temperature evolution (b) of an SMA bar under strain-controlled loadings. The loading-unloading cycle is generally divided into five phases: the loading of austenite (I), the forward A → M phase transition (II), unloading of martensite (III), the reverse M → A phase transition (IV), and unloading of austenite (V).

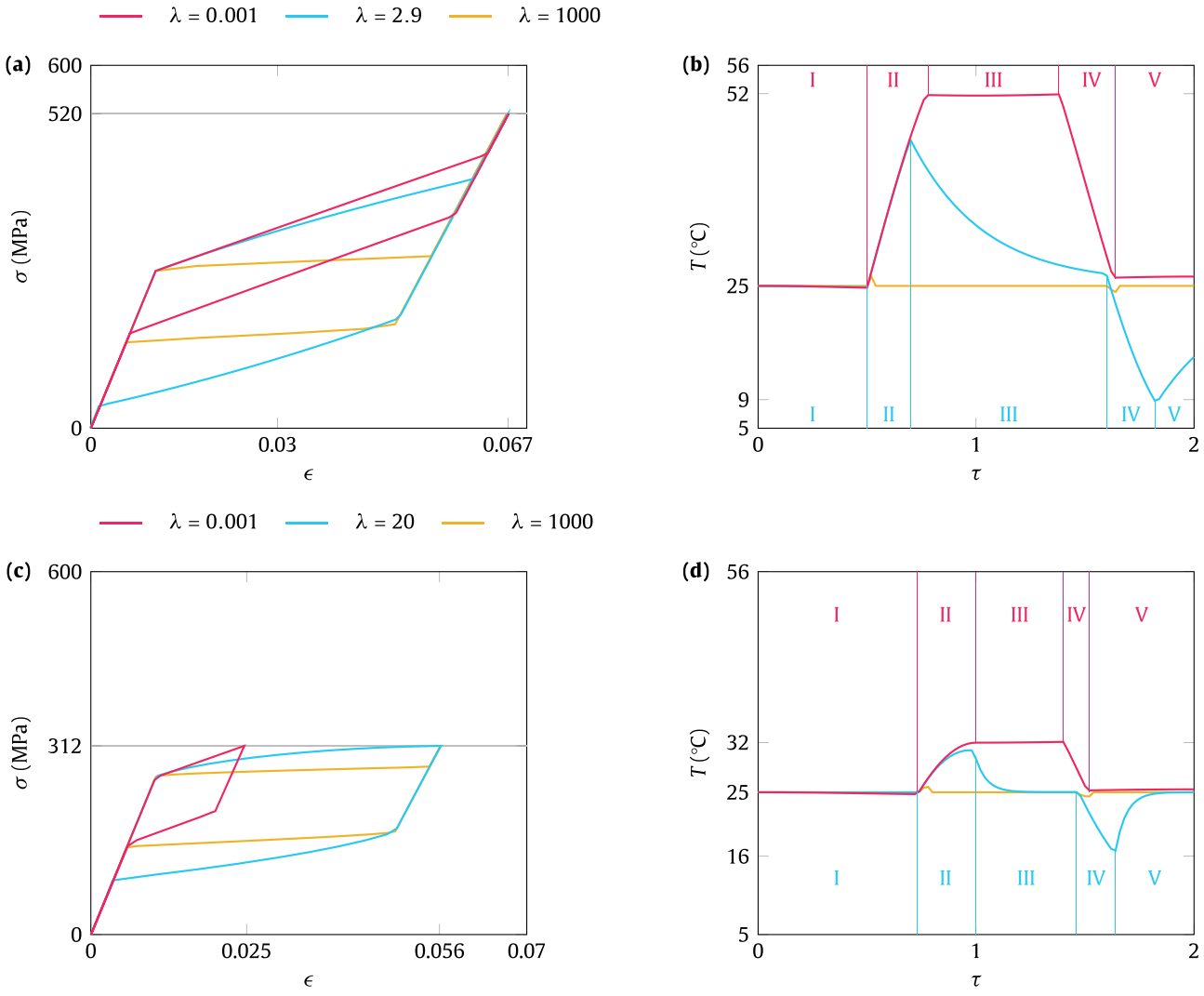

Fig. 4. Effects of the timescale ratio λ on the stress-strain (σ-ϵ) curve (a and c) and temperature evolution (b and d) of an SMA bar under stress-controlled loadings. The maximum stress ($\sigma_{\max}$ in Eq. (31a)) is 520 MPa for (a) and (b), and 312 MPa for (c) and (d). In panel b, the temperature evolution curve for $\lambda = 0.001$ is divided into five phases (in the upper): the loading of austenite (I), the forward A → M phase transition (II), loading and unloading of martensite (III), the reverse M → A phase transition (IV), and unloading of austenite (V). For $\lambda = 2.9$, the five phases I-V are denoted in the bottom. In panel d, the five phases for $\lambda = 20$ and 0.001 are referred to Fig. 3b.

the forward transition is not completely stored but largely transferred out. Third, during the unloading process of austenite (V), the temperature increases slightly because of the heat influx from the surroundings, but this compensation is so small that the final temperature after a full loading-unloading cycle is still lower than the room temperature. Finally, the transition stress is increasingly higher than the isothermal plateau stress in the forward phase transition but lower during the reverse phase transition. The enclosed hysteresis loop is thus larger than the isothermal one (it is the largest as shown in Fig. 5).

Fig. 4 shows results under the stress-controlled loadings. Here we consider two maximum stresses—520 MPa and 312 MPa—to show different change patterns of the stress strain curve against λ. The two maximum stress values actually correspond to the forces applied in experiments (Fig. 11). For the maximum stress 520 MPa, Fig. 4a and b show responses at three typical λ values that correspond to the three solid points D, E, and F in Fig. 5b. The observations in Fig. 3 also apply here, with a few differences. First, the maximum stress 520 MPa is as large as to ensure complete phase transitions at all the three λ values. Thus the stress and strain at the end of the forward phase transition (II) in Fig. 4a both increase from the isothermal to the adiabatic conditions (this accounts for the observation that the width of phase II for $\lambda = 2.9$ is smaller than that for $\lambda = 0.001$), while only the stress at the end of the forward transition increases in Fig. 3a. Second, the phase transition time is relatively shorter: phases II and IV in Fig. 4b are narrower than those in Fig. 3b (same loading function of time—Eqs. (31a) and (31b)—but smaller stress difference than strain difference (Fig. 6) between the start and finish of the phase transition). Finally, the forward phase transition at $\lambda = 2.9$ is so short that the temperature keeps growing at the same pace as that under the adiabatic condition during its whole phase transition process (bottom blue II), unlike the non-monotonic variation in Fig. 3b at $\lambda = 3.2$; this temperature behavior just corresponds to the initial stage of phase II in Fig. 3b. The subsequent temperature plummet in phase III leads to a non-smooth transition from phase II to III.

Unlike the case in Fig. 4a and b, the lower level of maximum stress 312 MPa induces different responses in Fig. 4c and d (the three λ values correspond to the three solid points G, H, and I in Fig. 5c). First, as λ decreases to 20, the phase transition starts to become incomplete. With further decrease of the λ value, the stress strain curve drifts to the left-hand side (instead of upwards in Fig. 4a), and the fraction of the phase transition shrinks. Second,

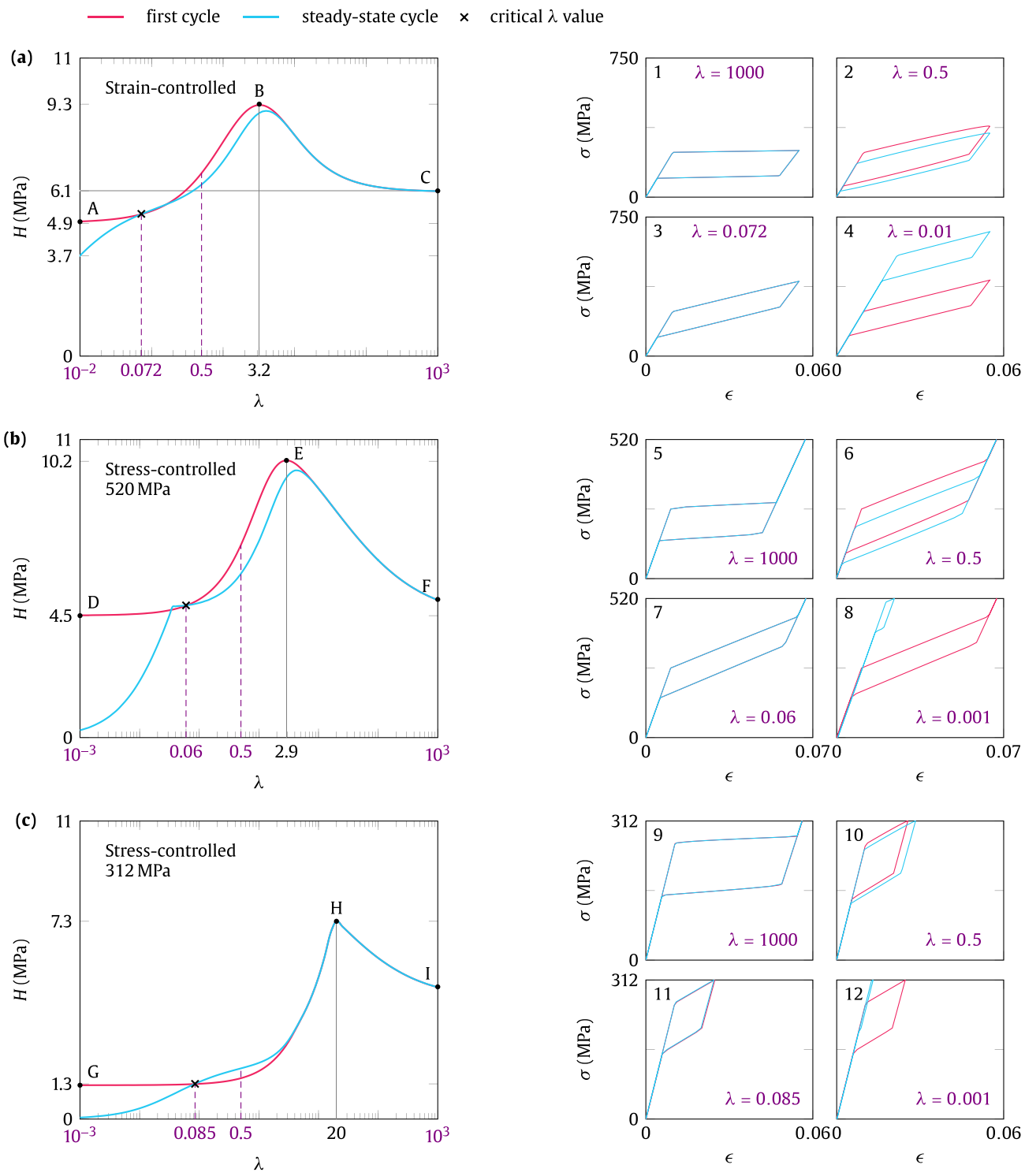

Fig. 5. Effects of the timescale ratio λ on damping capacity H (hysteresis loop area) of the first and steady-state cycles for strain-controlled (a) and stress-controlled (b and c) loadings. A–C, D–F, and G-I correspond to the three typical λ values in Figs. 3, 4a, and 4c, respectively. For each plot in the left-hand side, there are four subplots in the right-hand side showing the first-cycle and steady-state-cycle stress-strain (σ-ϵ) curves at four highlighted λ values (1 – 4 for (a), 5 – 8 for (b), and 9 – 12 for (c)). The critical λ value denoted by the cross is the one at which the mean temperature remains constant and the stress strain curves of all cycles coincide with each other (subplot 3, 7, and 11). In subplots 1, 3, 5, 7, 9, and 11, stress strain curves of the first (red) and steady-state-cycles (blue) coincide. The steady-state hysteresis (blue lines) will be compared with experimental data in Fig. 11.

the lower stress limit also changes the λ value for the biggest hysteresis loop from 2.9 to 20, at which the finish stress σ_{Mf} of the forward phase transition equals the maximum stress 312 MPa. Finally, the incomplete forward phase transition (II) for $\lambda = 20$ lasts as long as that for $\lambda = 0.001$, and the temperatures for the two λ values are close to each other, due to the synchronized increase of phase transition stress in phase II. Apparently, the temperature increase under the adiabatic condition in Fig. 4d is smaller than that in Fig. 4b because of the incomplete phase transition.

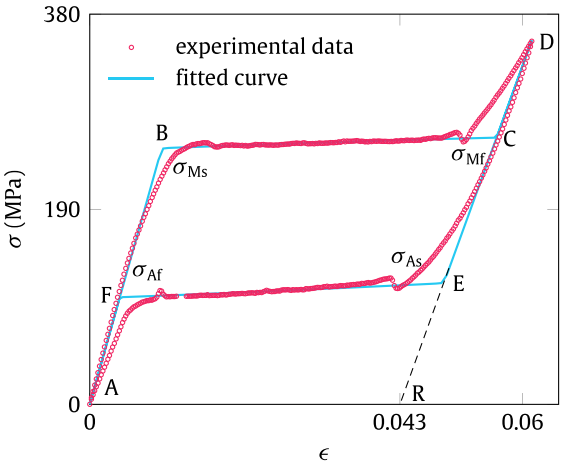

Fig. 6. Experimental (Yin et al., 2014) and fitted stress-strain (σ-ϵ) curves of an SMA bar under isothermal (25 °C) condition.

3.2.2. On damping capacity

An important quantity of SMAs is the damping capacity, which is the hysteresis loop area in the stress strain curve of a loading-unloading cycle. As shown in Figs. 3 and 4, the maximum damping capacity occurs at an intermediate λ value, in agreement with the non-monotonic variation of hysteresis *versus* the loading frequency in experimental studies (He et al., 2010; Yin et al., 2013, 2014; Morin et al., 2011a, 2011b; He and Sun, 2011). Here we systematically show the variation of hysteresis as a function of the timescale ratio λ under strain-controlled (Fig. 5a) and stress-controlled (Fig. 5b and c) loadings. For each loading case, we show the hysteresis of the first and steady-state cycles. It is remarked that for lower λ values, it takes more cycles for the thermo-mechanical responses to reach the steady state.

For the strain-controlled case (Fig. 5a), the first-cycle hysteresis (red line) shows a bell shape with the peak value at $\lambda = 3.2$; this λ value suggests that the maximum damping capacity is obtained when the loading timescale is close to the characteristic timescale of heat transfer. Very close timescale ratios are reported in experiments: around 1 in He et al. (2010) and He and Sun (2011) and around 2 in Yin et al. (2013). Although specific materials considered in these three references are not the same as in this study, the governing mechanism of timescale competition leads to comparable λ values for the peak damping capacities. As λ grows to 1000, the first-cycle hysteresis approaches the isothermal value 6.1 MPa (C), which is about 34% lower than the peak hysteresis 9.3 MPa (B); as λ decreases to 0.01, the first-cycle hysteresis gets close to the adiabatic value 4.9 MPa (A), which is around 47% less than the peak value.

In Fig. 5a, the hysteresis of the steady-state cycle is always not greater than the first-cycle hysteresis and is maximized at a higher λ value. To gain insights into this observation, we pick four λ values (1000, 0.5, 0.072, and 0.01) and plot the stress strain curves of the first and steady-state cycles in the right-hand side. Under the approximately isothermal condition ($\lambda = 1000$), the two stress strain curves completely coincide (subplot 1) because the temperature remains constant. At $\lambda = 0.5$, the heat transfer with the ambient environment makes the bar temperature lower than the room temperature after the first loading-unloading cycle (see Fig. 3b when $\lambda = 3.2$). After hundreds of cycles, the heat loss will accumulate leading to decreasing mean temperature (*i.e.*, average of the oscillating temperature; see Fig. 8 and Yin et al. (2014)). The decreasing temperature causes the stress strain curve to drift downwards and the hysteresis to shrink (subplot 2). However, when λ decreases to the critical value 0.072 (an equivalent critical frequency is observed in experiments of Yin et al. (2014)), the temperature goes back to the room temperature after the first loading-unloading cycle. Therefore, the following cycles will repeat the first one, and all the stress strain curves coincide with each other (subplot 3). At $\lambda = 0.01$, the temperature is higher than the room temperature after the first loading-unloading cycle (Fig. 3b); therefore, the accumulated heat will further grow in the following cycles and make the stress strain curve drift upwards with reducing hysteresis loop area as shown in subplot 4.

Fig. 5b shows the hysteresis under stress-controlled loading with the maximum stress of 520 MPa. The first-cycle hysteresis (red line) displays a similar variation pattern to its counterpart in the strain-controlled case (Fig. 5a), and the λ value 2.9 for the peak point is very close to the value 3.2 in Fig. 5a. Moreover, the steady-state-cycle hysteresis is also not greater than the first-cycle hysteresis, in agreement with experiments (Morin et al., 2011b) that report decreasing hysteresis with loading cycles under force controls. The difference between Fig. 5b and 5a comes when λ decreases to the critical value $\lambda = 0.06$: the steady-state-cycle hysteresis starts to plummet showing a non-smooth transition in Fig. 5b. This phenomenon can be accounted for by subplot 8: due to the maximum stress restriction, the stress strain curve drifts to the left-hand side (instead of upwards as in subplot 4) and the fraction of phase transition decreases with loading cycles.

Although non-monotonic, the hysteresis in Fig. 5c for the lower maximum stress 312 MPa shows different features. First, the hysteresis of the first and steady-state cycles are both lower than their counterparts in Fig. 5b. This is simply because the lower the maximum stress, the less the forward phase transition proceeds (subplot 6 *versus* 10, 7 *versus* 11, and 8 *versus* 12). Second, at $\lambda = 0.5$ the hysteresis of the steady-state cycle is higher than that of the first cycle, contrary to the observation in Fig. 5a and b. This can be seen in subplot 10: the stress strain curve drifts to the right-hand side from the first cycle to the steady-state cycle due to the lower maximum stress, different from going downwards in subplots 2 and 6. Finally, the hysteresis transition at the peak point (H) is not smooth. Consider the first-cycle hysteresis, whose peak value occurs at $\lambda = 20$. As shown by Fig. 4c, with decreasing λ, the stress strain curve drifts to the left-hand side, while it drifts downwards with increasing λ. This contrasting change pattern is responsible for the different hysteresis change trends in the two sides of the peak point.

4. Comparison with experiments

This section applies the coupled model to simulate experiments for the purpose of validation. We first calibrate model parameters using the data of isothermal tests of NiTi SMAs in Yin et al. (2014) and Yin (2013), and then compare model predictions with experimental results (Yin et al., 2014), in terms of stress strain curves, temperature evolution, and hysteresis loop area under various loading frequencies.

4.1. Model parameter calibration

In Fig. 6, red circles show the isothermal (at room temperature 25 °C) stress strain curve of an SMA bar subjected to uniaxial tension (Yin et al., 2014), while the solid blue line is the fitted curve by the coupled model. Here the isothermal condition is maintained by a very low loading frequency. It is shown that external loading first causes the elastic tension of austenite (AB), and further loading leads to the forward phase transition from austenite to martensite (BC), followed by elastic loading of martensite (CD). Reverse loading causes elastic unloading of martensite (DE), and continued unloading is accompanied by the reverse phase transition (EF) and subsequent elastic unloading of austenite (FA).

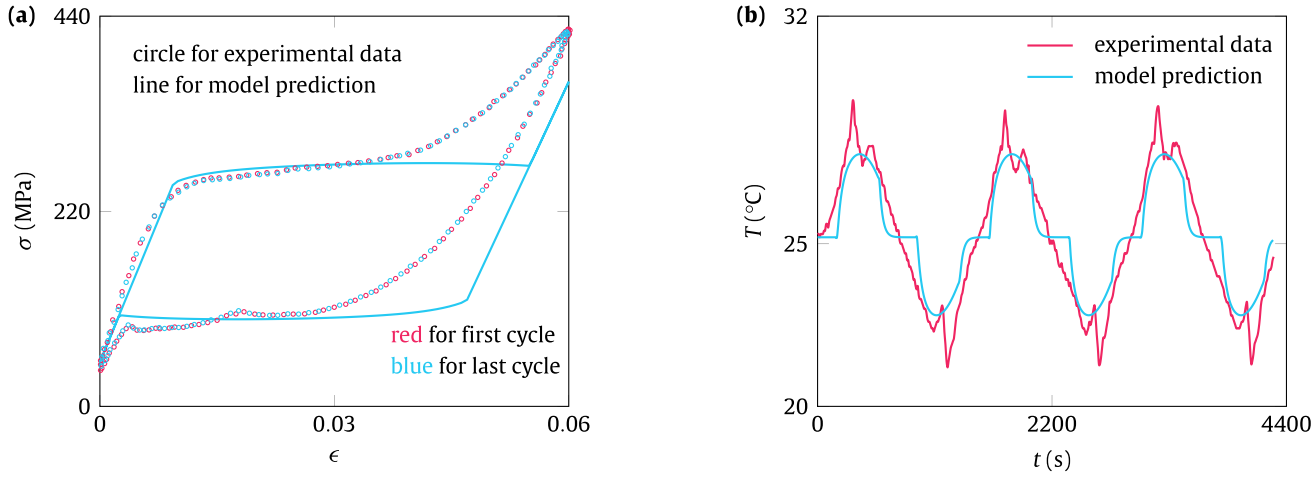

Fig. 7. Stress-strain (σ-ϵ) curves of the first and last cycles (a) and temperature evolution (b) at a low frequency 0.0007 Hz for displacement-controlled cyclic loading. In panel (a), the red solid line is covered by the blue line. Experimental data are from Yin et al. (2014).

From the experimental stress strain curve, we directly obtain the following parameters: Young's modulus of austenite E_A (slope of AB), Young's modulus of martensite E_M (slope of DCE), and the transformation strain ϵ_L, which is estimated at the intersection point (R) of dashed line ER (the unloading line of martensite) with the strain axis. Also, we can obtain the four transformation stresses (σ_{Ms}, σ_{Mf}, σ_{As}, and σ_{Af}, associated with points B, C, E, and F, respectively) at room temperature 298 K, and then the four transformation temperatures (M_s, M_f, A_s, and A_f) in stress-free state are readily interpolated from Fig. 2a, given the slope k.

The slope k (the coefficient in Clausius-Clapeyron relation) can be obtained from Fig. 11 of Yin et al. (2014) by calculating the dependence of transformation stress on temperature from many isothermal tensile tests at different temperatures. The entropy difference at the reference state is then calculated by Eq. (22). The specific heat capacity c_σ can be found in Yin et al. (2014) and the coefficient of thermal expansion α is from Table 5.1 of Lagoudas (2008). These parameters are used to fit our model to the experimental isothermal stress strain curve, and the fitted curve well captures the trend of the experimental curve. All calibrated parameters are summarized in Table 2.

4.2. Displacement-controlled cyclic loading

Pronounced coupling phenomena have been observed especially in cyclic loading-unloading of SMA bars at various loading frequencies (Yin et al., 2014). In the following, we compare predicted thermo-mechanical responses by our model with experimental data of displacement-controlled cyclic tests in Yin et al. (2014). Specifically, the cyclic stress strain curves and temperature evolution are of interest. In experiments, the displacement u is prescribed as

$$u = \frac{u_{\max}}{2}(1 - \cos 2\pi f t), \tag{36}$$

where $u_{\max}$ is the maximum displacement and f is the loading frequency, related to the angular frequency by $\omega = 2\pi f$. For model prediction, the parameters used are those in Table 2. The ambient temperature T_0 is kept constant at room temperature 25 °C. Next, results at three different loading frequencies f are compared.

Fig. 7 shows the stress strain curves of the first and last cycles (3 cycles in total) and temperature evolution at a low frequency 0.0007 Hz. For the numerical simulation, the characteristic time of heat transfer takes $t_h = 31$ s according to Fig. 3 in Yin et al. (2014); the timescale ratio is thus calculated as $\lambda = 23$. Since the loading-unloading is much slower than the heat transfer, the temperature varies slightly and goes back to the room temperature after the forward and reverse phase transitions in the simulation. The temperature variations in all loading-unloading cycles are the same, and hence the stress strain curves of the three cycles coincide with each other. A discrepancy between the model prediction and experimental results in Fig. 7a is that, the stress during the forward phase transition monotonically increases in experiments but deceases at the end of the forward phase transition according to the simulation. This stress decrease in model prediction is caused by the temperature decrease (Fig. 7b) in the latter half of the forward transition: according to Clausius-Clapeyron relation, the transformation stress decreases with a temperature decrease.

Fig. 8 shows the stress strain curves and temperature evolution at an intermediate frequency 0.04 Hz. For the numerical simulation, we take $t_h = 30$ s (Yin et al., 2014) and hence $\lambda = 0.42$. The temperature variation in Fig. 8b shows an evolution from the transient stage to the steady state with decreasing mean temperature. After the first cycle the temperature is lower than the room temperature because the heat transfer is neither as strong as to compensate the latent heat absorption in the reverse phase transition (as occurs in Fig. 7) nor as weak as to save the latent heat released in the forward phase transition (as occurs in Fig. 9). With increasing loading cycles, the temperature decrease accumulates and finally reaches an equilibrium. Due to the temperature decrease, the stress strain curve drifts downwards in Fig. 8a because of the temperature dependence of the transformation stress (Clausius-Clapeyron relation).

Fig. 9 shows the thermo-mechanical responses at a high frequency 1 Hz. In numerical simulation we use $t_h = 26$ s (Yin et al., 2014) and hence $\lambda = 0.02$. The λ value is so small that the heat transfer with the ambient environment can be disregarded (*i.e.*, adiabatic condition). Thus the temperature in Fig. 9b oscillates due to the latent heat release and absorption in the reversible phase transitions. The mean temperature keeps increasing because of the accumulation of hysteresis heat. The thermal effect on the mechanical responses reflects in the upward shift of the stress strain curve from Fig. 9a to b. It can be seen that our model can capture essential features of the temperature evolution and the trend of the stress strain curve change.

4.3. Force-controlled cyclic loading

Besides the displacement-controlled tests, we further compare our model prediction with experimental data from force-controlled

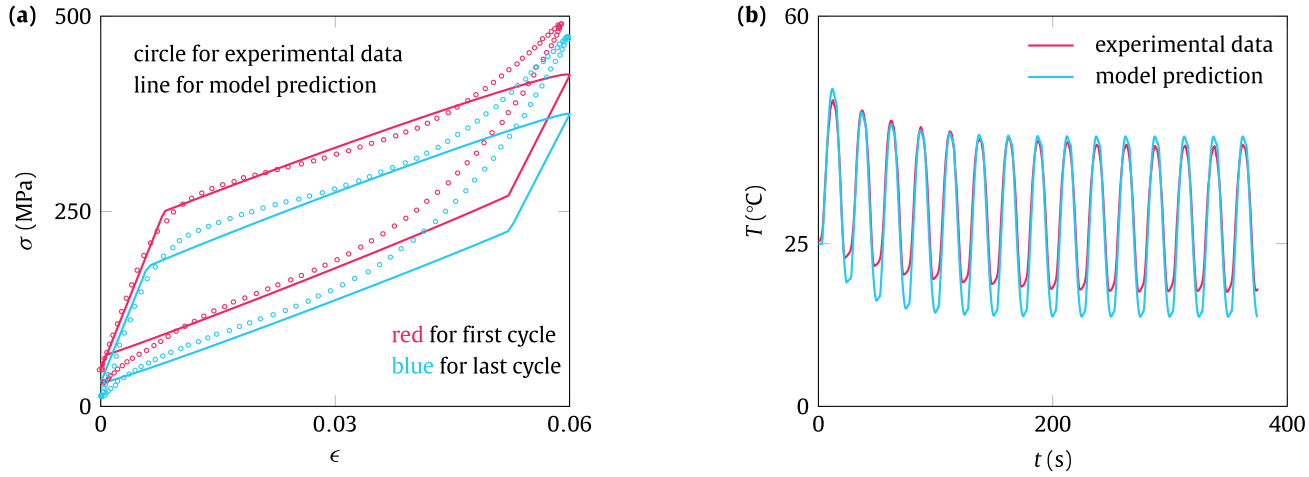

Fig. 8. Stress-strain (σ-ϵ) curves of the first and last cycles (a) and temperature evolution (b) at an intermediate frequency 0.04 Hz for displacement-controlled cyclic loading. Experiment data are from Yin et al. (2014).

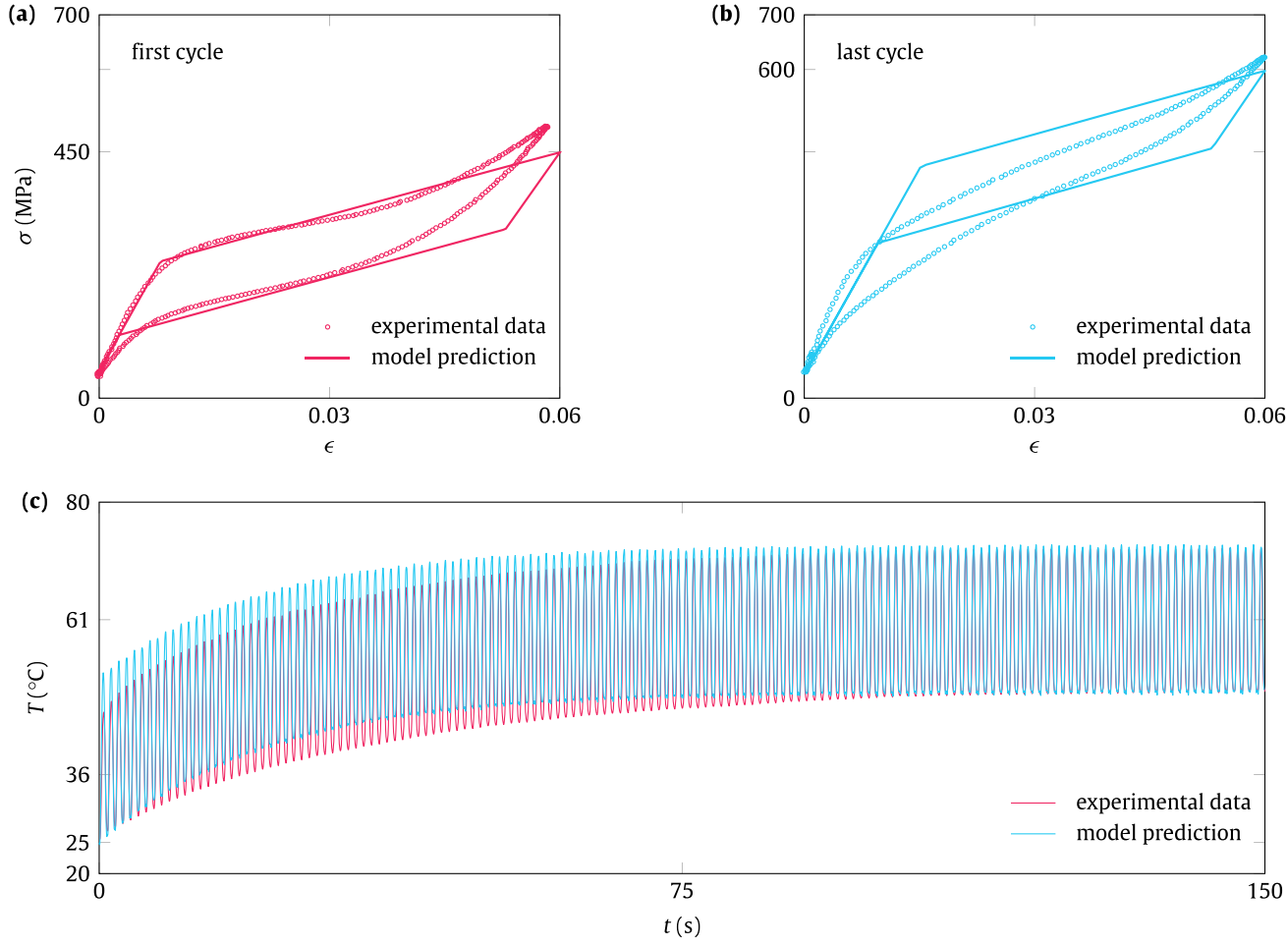

Fig. 9. Stress-strain (σ-ϵ) curves of the first and last cycles (a) and temperature evolution (b) at a high frequency 1 Hz for displacement-controlled cyclic loading. Experiment data are from Yin et al. (2014).

cyclic tests by Yin (2013). The axial force F is specified as

$$F = \frac{F_{\max}}{2}(1 - \cos 2\pi f t), \tag{37}$$

where $F_{\max}$ is the maximum force applied. Here we consider the loading frequency of 1 Hz. The stress strain curves of the first and last (steady-state) cycles and the temperature evolution are shown in Fig. 10. Considering that the specimens for force-controlled tests in Yin (2013) might not be the same batch as those for displacement-controlled tests in Yin et al. (2014), we recalibrate some parameters by fitting the first-cycle stress strain curve; the updated (compared to Table 2) model parameters are separately

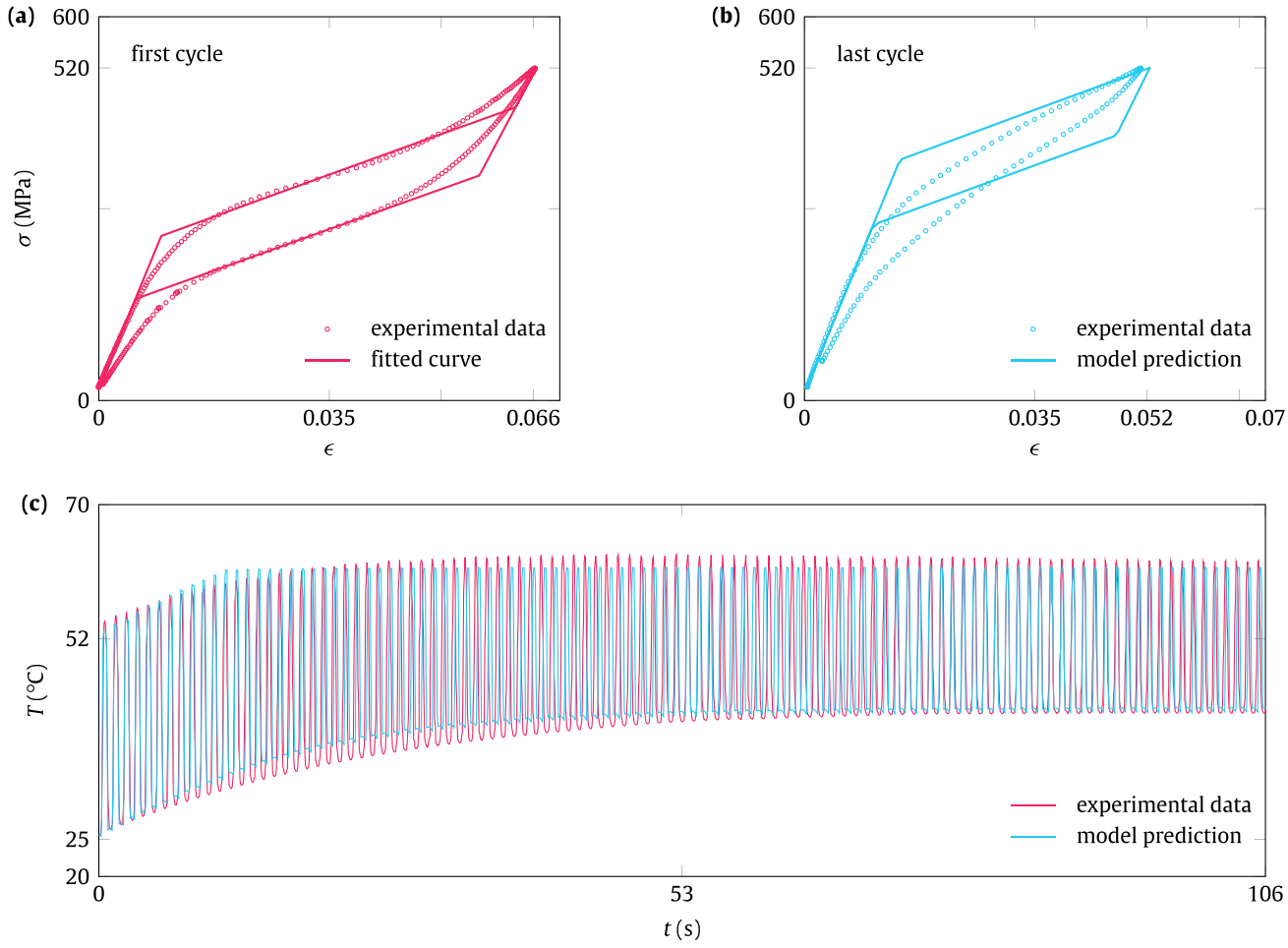

Fig. 10. Stress-strain (σ-ϵ) curves of the first and last cycles (a) and temperature evolution (b) at loading frequency 1 Hz for force-controlled cyclic loading. Experiment data are from Yin (2013).

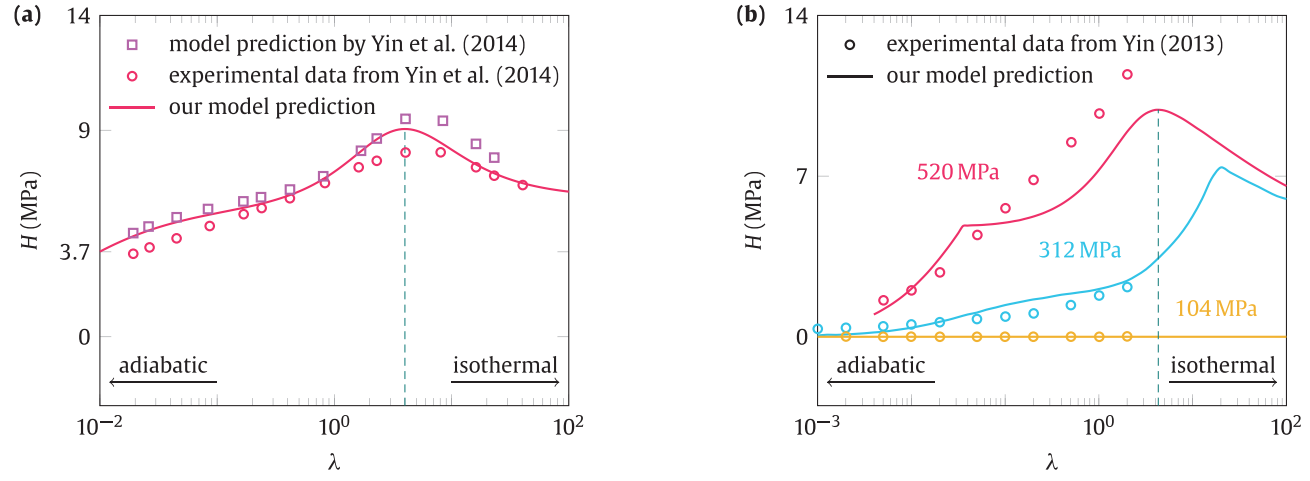

Fig. 11. Comparison of our model prediction with experimental data in terms of the damping capacity H (stress strain hysteresis) of the steady-state cycle *versus* the dimensionless timescale ratio λ. Panel (a) is for displacement-controlled loading while panel (b) is for force-controlled loading. The three stress values (520 MPa, 312 MPa, and 104 MPa) correspond to the maximum forces $F_{\max} = 5000$ N, 3000 N, and 1000 N applied in experiments (Eq. (37)), respectively.

listed in Table 3 but those not changed are omitted. We then use the updated parameters to predict the stress strain curve of the last cycle (Fig. 10b) and temperature evolution (Fig. 10c). The model is able to capture the drift of stress strain curve to the left-hand side (Fig. 10b) due to the increase of temperature and hence the transition stress.

4.4. Damping capacity

In Fig. 11, we compare the hysteresis of the steady-state cycle between our model prediction and experimental data (Yin et al., 2014; Yin, 2013). Fig. 11a shows results for the displacement-controlled cyclic loading. Our model prediction (red

line) is based on the calibrated parameters in Table 2. The experimental data (circles) are adapted from Yin et al. (2014): the hysteresis is shown against the loading frequency in Yin et al. (2014); here we convert the frequency to the timescale ratio λ by taking into account the measured characteristic time of heat transfer in Fig. 3 of Yin et al. (2014). It can be seen that our model prediction captures the non-monotonic variation of the hysteresis and obtain almost the same λ value for the peak hysteresis as the experimental one. Moreover, the predicted hysteresis curve especially agrees well with the experimental results under approximately isothermal conditions (high λ values). This better agreement may be because we calibrate the model parameters against the isothermal test.

Fig. 11b shows the comparison under force-controlled cyclic loading. Model parameters are from Table 3 and the experimental data are adapted from Yin (2013). At a high level of maximum stress 520 MPa, the experimental data are absent at some low loading frequencies (high λ values) and thus unable to show the usual non-monotonic hysteresis variation. The non-monotonic variation pattern is however seen in our model prediction with data available at high λ values. We believe in the predicted trend as λ increases beyond the experimental data, considering the agreement at high λ values in Fig. 11a. Likewise, our model prediction in the case of maximum stress 312 MPa agrees with the experimental data and demonstrates the trend and variation of hysteresis at higher λ values. At a low level of maximum stress 104 MPa, the hysteresis is always null from the model prediction and experimental results. The null hysteresis is simply because there is no phase transition incurred during the cyclic loading.

In Fig. 11a, we also include the model prediction (squares) made by the authors of Yin et al. (2014). Their prediction shows the same variation trend as ours, especially in the left-hand side of the peak point. The model by Yin et al. (2014) mainly focused on temperature evolution prediction and hysteresis evaluation. The heat equation required known material parameters representing the latent heat l_0 and hysteresis heat D_s. The release rates of the two heat sources should also be assumed to reflect the loading (displacement-controlled) rate. These assumptions permitted them to obtain an analytical temperature solution, consisting of the mean temperature evolution and an oscillating term. The coupled model in this study, however, directly simulates external loadings (displacement-controlled or force-controlled) and thus avoids assuming concrete forms of these heat release rates. The latent heat and hysteresis are calculated from the simulated results, rather than a priori model parameters, in the post-processes. If the latent heat $T\Delta s_0\dot{\xi}$ and hysteresis $\Pi\dot{\xi}$ in Eq. (29) are further simplified and related to the strain rate, we will obtain a heat equation similar to the one in Yin et al. (2014) and corresponding analytical solutions.

5. Conclusion

We present a thermo-mechanically coupled model for one-dimensional NiTi SMA bars. As indicated by the heat equation (29), the latent heat is due to the entropy difference between the martensite and austenite, and it serves as a heat source in A → M phase transition but a heat sink in M → A transition; the hysteresis is attributed to the non-equilibrium thermodynamic driving force and keeps converting mechanical energy to thermal energy. Scaling the governing equations enables us to derive a dimensionless number—the timescale ratio λ (Eq. (35)) that expresses the competition between the loading time and the characteristic time of heat transfer. The identification of λ in the coupled model suggests that the two-timescale competition is responsible for the thermo-mechanical responses.

By exploring λ within a wide range of numbers, we have a full picture of the thermo-mechanical responses (Figs. 3 and 4) under different combinations of external loading, ambient conditions, and the specimen geometry, encompassing conditions from the isothermal case to adiabatic case. Under the cyclic loading, the first-cycle hysteresis is generally higher than (at low λ values) or equal to (at high λ values) that of the steady-state cycle (Fig. 5a and b). For both the stress- and strain-controlled cases, the damping capacity of the first cycle is maximized when λ value is around 3; the steady-state-cycle damping capacity is maximized at a slightly higher λ value. Nevertheless, these observations do not completely apply to the particular case of incomplete phase transition under force-controlled loadings (Fig. 5c): the maximum applied stress also affects the λ value leading to the maximum damping capacity.

The thermo-mechanically coupled model is validated by comparison with experimental results of an SMA bar under displacement and force controls. The timescale ratio λ can thus provide guidelines for setting experimental conditions to achieve desired responses.

Declaration of Competing Interest

The authors declare that they have no known competing financial interests or personal relationships that could have appeared to influence the work reported in this paper.

Acknowledgments

The author is grateful for the financial support from the Hong Kong Research Grant Council through Grant No. N_HKUST 617/14. The author would also like to give special thanks to Dr. Yin Hao for his kind sharing of published experimental data.

Appendix A. Thermodynamic basics

We apply the second law of thermodynamics to an arbitrary fixed control volume Ω with boundary denoted as ∂Ω: the entropy production should be always non-negative, which can be expressed by the Clausius-Duhem inequality (Lagoudas, 2008)

$$\int_\Omega \dot{s}\ \mathrm{d}V + \int_{\partial\Omega} \frac{\mathbf{q}}{T}\cdot\mathbf{n}\ \mathrm{d}S - \int_\Omega \frac{r}{T}\ \mathrm{d}V \geq 0, \tag{A.1}$$

where s is the entropy per unit volume, T is the absolute temperature, $\mathbf{q}$ is the heat flux vector, $\mathbf{n}$ is the outward-pointing unit vector normal to the volume surface ∂Ω, and r is the heat source per unit volume. Applying the divergence theorem to the surface integral term and summing everything together within a common volume integral, we obtain the local form of the Clausius-Duhem inequality:

$$\dot{s} + \frac{1}{T}\nabla\cdot\mathbf{q} - \frac{1}{T^2}\mathbf{q}\cdot\nabla T - \frac{r}{T} \geq 0, \tag{A.2}$$

in view of the arbitrariness of control volume Ω. Multiplying T at both sides of Eq. (A.2) yields

$$D = T\dot{s} + \nabla\cdot\mathbf{q} - \frac{1}{T}\mathbf{q}\cdot\nabla T - r \geq 0, \tag{A.3}$$

where D is the dissipation in the irreversible thermodynamic processes. Usually, we can further split the total dissipation D into non-zero mechanical dissipation

$$D_\mathrm{m} = T\dot{s} + \nabla\cdot\mathbf{q} - r \geq 0 \tag{A.4}$$

and non-zero thermal dissipation

$$D_\mathrm{t} = -\frac{1}{T}\mathbf{q}\cdot\nabla T \geq 0 \tag{A.5}$$

to express the strict forms of the second law of thermodynamics; Eqs. (A.4) and (A.5) are conventionally called Clausius-Planck inequality and Fourier inequality, respectively. The mechanical dissipation inequality (A.4) will be used in the following to derive the constitutive relations.

The first law of thermodynamics states that the rate of internal energy change of a system is equal to the rate at which external work done on the system, plus the rate of heat influx and heat generation. The local form of the first law is given by

$$\dot{u} = \boldsymbol{\sigma} : \dot{\boldsymbol{\epsilon}} - \nabla \cdot \mathbf{q} + r, \tag{A.6}$$

where u is the internal energy per unit volume (specific internal energy), $\boldsymbol{\sigma} : \dot{\boldsymbol{\epsilon}}$ is the stress power per unit volume. From the relation between the specific internal energy u and specific Gibbs free energy g

$$g = u - \boldsymbol{\sigma} : \boldsymbol{\epsilon} - Ts,$$

we obtain the time rate of change of g:

$$\dot{g} = \dot{u} - \dot{\boldsymbol{\sigma}} : \boldsymbol{\epsilon} - \boldsymbol{\sigma} : \dot{\boldsymbol{\epsilon}} - \dot{T}s - T\dot{s}. \tag{A.7}$$

Substituting Eq. (A.6) into (A.7) and considering Eq. (A.4) yield

$$\dot{g} = -\dot{\boldsymbol{\sigma}} : \boldsymbol{\epsilon} - \dot{T}s - D_{\mathrm{m}}. \tag{A.8}$$

The specific Gibbs free energy g can be considered as a state function of a set of state variables and internal variables (Coleman and Gurtin, 1967) and its time derivative can be expressed as

$$\dot{g} = \frac{\partial g}{\partial \boldsymbol{\sigma}} : \dot{\boldsymbol{\sigma}} + \frac{\partial g}{\partial T}\dot{T} + \frac{\partial g}{\partial \boldsymbol{\zeta}} : \dot{\boldsymbol{\zeta}}, \tag{A.9}$$

where $\boldsymbol{\sigma}$ and T are the state variables and $\boldsymbol{\zeta}$ is the internal variable(s). Equating (A.8) to (A.9), we obtain the expression of the mechanical dissipation D_{m}:

$$D_{\mathrm{m}} = -\left(\boldsymbol{\epsilon} + \frac{\partial g}{\partial \boldsymbol{\sigma}}\right) : \dot{\boldsymbol{\sigma}} - \left(s + \frac{\partial g}{\partial T}\right)\dot{T} - \frac{\partial g}{\partial \boldsymbol{\zeta}} : \dot{\boldsymbol{\zeta}} \geq 0. \tag{A.10}$$

Since $\boldsymbol{\sigma}$ and T are arbitrary independent variables, to satisfy the Clausius-Planck inequality (A.10) we have to make

$$\boldsymbol{\epsilon} = -\frac{\partial g}{\partial \boldsymbol{\sigma}}, \quad s = -\frac{\partial g}{\partial T}, \tag{A.11}$$

which are the constitutive relations for the state variables. In the one-dimensional case, the stress and strain tensor in Eq. (A.11) are reduced to scalars (*i.e.*, the axial stress and strain).

Appendix B. Evolution rules for incomplete phase transitions

The linear evolution rules (Eq. (21), Fig. 2b) assume complete forward and reverse phase transitions. Here we add evolution rules for incomplete phase transitions—unloading before the forward phase transition completes and reloading before the reverse phase transition completes. To this end, an inner reversible path IJ in Fig. 2b is assumed as the loading and unloading paths.

The vertical inner path in $\Gamma - \xi$ diagram (Fig. 2b) indicates that the martensite volume fraction ξ does not change on the path until the outer path is met. Hence, the evolution rules in Eq. (21) does not change but the range of the control driving force Γ for phase transitions becomes narrower. To reflect this change, we introduce two extra variables—$\xi_{\min}$ and $\xi_{\max}$—to record the loading history. The two variables ($\xi_{\min}$ and $\xi_{\max}$) denote, respectively, the minimum martensite volume fraction reached in the reverse phase transition before a reloading starts and the maximum martensite volume fraction reached in the forward phase transition before an unloading starts. The complete evolution rule can now be expressed in a rate form as follows.

1. when $\dot{\Gamma} > 0$ and $\xi_{\min}(M_{\mathrm{s}} - M_{\mathrm{f}})\Delta s_0 - M_{\mathrm{s}}\Delta s_0 < \Gamma < -M_{\mathrm{f}}\Delta s_0$,

$$\dot{\xi} = \frac{\dot{\Gamma}}{(M_{\mathrm{s}} - M_{\mathrm{f}})\Delta s_0}, \tag{B.1a}$$

2. when $\dot{\Gamma} < 0$ and $-A_{\mathrm{s}}\Delta s_0 < \Gamma < \xi_{\max}(A_{\mathrm{f}} - A_{\mathrm{s}})\Delta s_0 - A_{\mathrm{f}}\Delta s_0$,

$$\dot{\xi} = \frac{\dot{\Gamma}}{(A_{\mathrm{f}} - A_{\mathrm{s}})\Delta s_0}, \tag{B.1b}$$

3. otherwise,

$$\dot{\xi} = 0. \tag{B.1c}$$

It is remarked that $\xi_{\min}$ should be updated in the reverse phase transition and $\xi_{\max}$ updated in the forward phase transition.

Table C.4
Numerical algorithm for stress-controlled loading.

1. Given: admissible point $(\sigma_n, \epsilon_n, T_n, \xi_n)$ and σ_{n+1}.
2. Compute elastic trial state:
   $\xi_{n+1}^{\mathrm{trial}} = \xi_n$,
   $T_{n+1}^{\mathrm{trial}} = T_n - \frac{\alpha}{c_\sigma} T_n(\sigma_{n+1} - \sigma_n) - \lambda(T_n - T_0)\Delta t$,
   $\Gamma_{n+1}^{\mathrm{trial}} = \sigma_{n+1}\epsilon_{\mathrm{L}} - T_{n+1}^{\mathrm{trial}}\Delta s_0$.
3. Test for phase transition:
   If $\Gamma_{n+1}^{\mathrm{trial}} > \Gamma_n$ **then**
   If $\xi_{\min}(M_{\mathrm{s}} - M_{\mathrm{f}})\Delta s_0 - M_{\mathrm{s}}\Delta s_0 < \Gamma_n < -M_{\mathrm{f}}\Delta s_0$ **then**
   substitute (C.3) into (C.2) to solve for T_{n+1} and then ξ_{n+1},
   update $\xi_{\max} = \xi_{n+1}$,
   Else the trial state is the actual state;
   Else If $-A_{\mathrm{s}}\Delta s_0 < \Gamma_n < \xi_{\max}(A_{\mathrm{f}} - A_{\mathrm{s}})\Delta s_0 - A_{\mathrm{f}}\Delta s_0$ **then**
   substitute (C.4) into (C.2) to solve for T_{n+1} and then ξ_{n+1},
   update $\xi_{\min} = \xi_{n+1}$,
   Else the trial state is the actual state;
   Update $\Gamma_{n+1} = \sigma_{n+1}\epsilon_{\mathrm{L}} - T_{n+1}\Delta s_0$.
4. Compute strain ϵ_{n+1} based on Eq. (C.1).

Appendix C. Numerical solution

This section provides the numerical procedures to solve the nondimensionalized governing equations—the stress strain equation (8), heat equation (32), evolution rules (B.1), and prescribed loadings (31).

1. Suppose that an admissible point $(\sigma, \epsilon, \xi, T)$ and prescribed stress $\sigma = \sigma(\tau)$ (or strain $\epsilon = \epsilon(\tau)$) are given.
2. Assume a trial state in which no phase transition occurs ($\dot{\xi} = 0$), and then solve Eqs. (8) and (32) for the strain ϵ (or stress σ) and temperature T.
3. Calculate control driving force Γ and its rate change $\dot{\Gamma}$, and then check whether it satisfies the conditions for phase transition in Eq. (B.1). If not, the solution of the trial state is the actual solution;
4. otherwise, choose the evolution rule (21a) or (21b) based on $\dot{\Gamma}$ and solve it together with Eqs. (8) and (32).

The procedures just reported are called return mapping algorithm (Simo and Hughes, 1998). To numerically implement the procedures, we formulate the discretized forms of the coupled equations as follows.

1. The discretized form of the stress strain relation (8) is

$$\epsilon_{n+1} = \frac{\sigma_{n+1}}{E(\xi_{n+1})} + \xi_{n+1}\epsilon_{\mathrm{L}} + \alpha(T_{n+1} - T_0). \tag{C.1}$$

Table C.5
Numerical algorithm for stain-controlled loading.

1. Given: admissible point $(\sigma_n, \epsilon_n, T_n, \xi_n)$ and ϵ_{n+1}.
2. Compute elastic trial state:

$$\xi_{n+1}^{\text{trial}} = \xi_n,$$
$$T_{n+1}^{\text{trial}} = T_n - \frac{\alpha/c_\sigma T_n E\left(\xi_{n+1}^{\text{trial}}\right)(\epsilon_{n+1}-\epsilon_n) + \lambda(T_n - T_0)\Delta t}{1 - \alpha^2/c_\sigma T_n E\left(\xi_{n+1}^{\text{trial}}\right)},$$
$$\sigma_{n+1}^{\text{trial}} = E\left(\xi_{n+1}^{\text{trial}}\right)\left[\epsilon_{n+1} - \xi_{n+1}^{\text{trial}}\epsilon_{\text{L}} - \alpha\left(T_{n+1}^{\text{trial}} - T_0\right)\right],$$
$$\Gamma_{n+1}^{\text{trial}} = \sigma_{n+1}^{\text{trial}}\epsilon_{\text{L}} - T_{n+1}^{\text{trial}}\Delta s_0.$$

3. Test for phase transition:

If $\Gamma_{n+1}^{\text{trial}} > \Gamma_n$ **then**

If $\xi_{\min}(M_s - M_f)\Delta s_0 - M_s\Delta s_0 < \Gamma_n < -M_f\Delta s_0$ **then**

using iterative method to solve (C.1), (C.2), and (C.3) simultaneously for σ_{n+1}, ξ_{n+1}, and T_{n+1},

update $\xi_{\max} = \xi_{n+1}$,

Else the trial state is the actual state;

Else If $-A_s\Delta s_0 < \Gamma_n < \xi_{\max}(A_f - A_s)\Delta s_0 - A_f\Delta s_0$ **then**

using iterative method to solve (C.1), (C.2), and (C.4) simultaneously for σ_{n+1}, ξ_{n+1}, and T_{n+1},

update $\xi_{\min} = \xi_{n+1}$,

Else the trial state is the actual state;

Update $\Gamma_{n+1} = \sigma_{n+1}\epsilon_{\text{L}} - T_{n+1}\Delta s_0$.

2. Heat equation (32) is an ordinary differential equation, and its time difference approximation is

$$T_{n+1} - T_n = \frac{\sigma_{n+1}\epsilon_{\text{L}} + \Delta u_0 - \Lambda(2\xi_{n+1} - 1)}{c_\sigma}(\xi_{n+1} - \xi_n) - \frac{\alpha T_n}{c_\sigma}(\sigma_{n+1} - \sigma_n) - \lambda(T_n - T_0)\Delta t. \tag{C.2}$$

3. The discretized evolution rules (21) are expressed as follows: when $\Gamma_{n+1} > \Gamma_n$ and $\xi_{\min}(M_s - M_f)\Delta s_0 - M_s\Delta s_0 < \Gamma_n < -M_f\Delta s_0$,

$$\xi_{n+1} = \frac{\sigma_{n+1}\epsilon_{\text{L}} - T_{n+1}\Delta s_0 + M_s\Delta s_0}{(M_s - M_f)\Delta s_0}; \tag{C.3}$$

when $\Gamma_{n+1} < \Gamma_n$ and $-A_s\Delta s_0 < \Gamma_n < \xi_{\max}(A_f - A_s)\Delta s_0 - A_f\Delta s_0$,

$$\xi_{n+1} = \frac{\sigma_{n+1}\epsilon_{\text{L}} - T_{n+1}\Delta s_0 + A_f\Delta s_0}{(A_f - A_s)\Delta s_0}; \tag{C.4}$$

otherwise,

$$\xi_{n+1} = \xi_n. \tag{C.5}$$

If the stress is given (Eq. (31a)), the detailed algorithm is available in Table C.4; if the strain is given (Eq. (31b)), the algorithm is shown in Table C.5[1].

References

Abeyaratne, R., Kim, S.-J., 1997. Cyclic effects in shape-memory alloys: A one-dimensional continuum model. Int. J. Solids Struct. 34 (25), 3273–3289. doi:10.1016/S0020-7683(96)00213-2.

Armattoe, K., Bouby, C., Haboussi, M., Zineb, T.B., 2016. Modeling of latent heat effects on phase transformation in shape memory alloy thin structures. Int. J. Solids Struct. 88–89, 283–295. doi:10.1016/j.ijsolstr.2016.02.024.

Auricchio, F., Fugazza, D., Desroches, R., 2008. Rate-dependent thermo-mechanical modelling of superelastic shape-memory alloys for seismic applications. J. Intell. Mater. Syst. Struct. 19 (1), 47–61. doi:10.1177/1045389X06073426.

Auricchio, F., Sacco, E., 1997. A one-dimensional model for superelastic shape-memory alloys with different elastic properties between austenite and martensite. Int. J. Non Linear Mech. 32 (6), 1101–1114. doi:10.1016/S0020-7462(96)00130-8.

Auricchio, F., Sacco, E., 2001. Thermo-mechanical modelling of a superelastic shape-memory wire under cyclic stretchingbending loadings. Int. J. Solids Struct. 38 (34), 6123–6145. doi:10.1016/S0020-7683(00)00282-1.

Bernardini, D., Pence, T.J., 2002. Models for one-variant shape memory materials based on dissipation functions. Int. J. Non Linear Mech. 37 (8), 1299–1317. doi:10.1016/S0020-7462(02)00020-3.

Bernardini, D., Rega, G., 2017. Evaluation of different SMA models performances in the nonlinear dynamics of pseudoelastic oscillators via a comprehensive modeling framework. Int. J. Mech. Sci. 130, 458–475. doi:10.1016/j.ijmecsci.2017.06.023.

Boyd, J.G., Lagoudas, D.C., 1996. A thermodynamical constitutive model for shape memory materials. Part i. The monolithic shape memory alloy. Int. J. Plast. 12 (6), 805–842. doi:10.1016/S0749-6419(96)00030-7.

Brinson, L.C., 1993. One-dimensional constitutive behavior of shape memory alloys: Thermomechanical derivation with non-constant material functions and redefined martensite internal variable. J. Intell. Mater. Syst. Struct. 4 (2), 229–242. doi:10.1177/1045389X9300400213.

Brinson, L.C., Huang, M.S., 1996. Simplifications and comparisons of shape memory alloy constitutive models. J. Intell. Mater. Syst. Struct. 7 (1), 108–114. doi:10.1177/1045389X9600700112.

Bruno, O.P., Leo, P.H., Reitich, F., 1995. Free boundary conditions at Austenite-Martensite interfaces. Phys. Rev. Lett. 74, 746–749. doi:10.1103/PhysRevLett.74.746.

Christ, D., Reese, S., 2009. A finite element model for shape memory alloys considering thermomechanical couplings at large strains. Int. J. Solids Struct. 46 (20), 3694–3709. doi:10.1016/j.ijsolstr.2009.06.017.

Churchill, C.B., Shaw, J.A., Iadicola, M.A., 2009. Tips and tricks for characterizing shape memory alloy wire: Part 3—localization and propagation phenomena. Exp. Tech. 33 (5), 70–78. doi:10.1111/j.1747-1567.2009.00558.x.

Cisse, C., Zaki, W., Zineb, T.B., 2016. A review of constitutive models and modeling techniques for shape memory alloys. Int. J. Plast. 76, 244–284. doi:10.1016/j.ijplas.2015.08.006.

Coleman, B.D., Gurtin, M.E., 1967. Thermodynamics with internal state variables. J. Chem. Phys. 47 (2), 597–613. doi:10.1063/1.1711937.

Cotta, R.M., Mikhailov., M.D., 1997. Heat conduction: Lumped analysis, integral transforms, symbolic computation. John Wiley & Sons.

Entemeyer, D., Patoor, E., Eberhardt, A., Berveiller, M., 2000. Strain rate sensitivity in superelasticity. Int. J. Plast. 16 (10), 1269–1288. doi:10.1016/S0749-6419(00)00010-3.

Feng, P., Sun, Q., 2006. Experimental investigation on macroscopic domain formation and evolution in polycrystalline NiTi microtubing under mechanical force. J. Mech. Phys. Solids 54 (8), 1568–1603. doi:10.1016/j.jmps.2006.02.005.

Grabe, C., Bruhns, O.T., 2008. On the viscous and strain rate dependent behavior of polycrystalline NiTi. Int. J. Solids Struct. 45 (7), 1876–1895. doi:10.1016/j.ijsolstr.2007.10.029.

Grandi, D., Maraldi, M., Molari, L., 2012. A macroscale phase-field model for shape memory alloys with non-isothermal effects: Influence of strain rate and environmental conditions on the mechanical response. Acta Mater. 60 (1), 179–191. doi:10.1016/j.actamat.2011.09.040.

He, Y., Sun, Q., 2010. Frequency-dependent temperature evolution in NiTi shape memory alloy under cyclic loading. Smart Mater. Struct. 19 (11), 115014. doi:10.1088/0964-1726/19/11/115014.

He, Y., Sun, Q., 2010. Rate-dependent domain spacing in a stretched NiTi strip. Int. J. Solids Struct. 47 (20), 2775–2783. doi:10.1016/j.ijsolstr.2010.06.006.

He, Y., Sun, Q., 2011. On non-monotonic rate dependence of stress hysteresis of superelastic shape memory alloy bars. Int. J. Solids Struct. 48 (11), 1688–1695. doi:10.1016/j.ijsolstr.2011.02.017.

He, Y., Yin, H., Zhou, R., Sun, Q., 2010. Ambient effect on damping peak of NiTi shape memory alloy. Mater. Lett. 64 (13), 1483–1486. doi:10.1016/j.matlet.2010.03.068.

Hetnarski, R.B., Eslami, M.R., 2009. Thermal stresses—Advanced theory and applications. Springer Netherlands doi:10.1007/978-1-4020-9247-3.

Iadicola, M.A., Shaw, J.A., 2004. Rate and thermal sensitivities of unstable transformation behavior in a shape memory alloy. Int. J. Plast. 20 (4), 577–605. doi:10.1016/S0749-6419(03)00040-8.

Ivshin, Y., Pence, T.J., 1994. A thermomechanical model for a one variant shape memory material. J. Intell. Mater. Syst. Struct. 5 (4), 455–473. doi:10.1177/1045389X9400500402.

Jani, J.M., Leary, M., Subic, A., Gibson, M.A., 2014. A review of shape memory alloy research, applications and opportunities. Materials & Design (1980–2015) 56, 1078–1113. doi:10.1016/j.matdes.2013.11.084.

Lagoudas, D., Hartl, D., Chemisky, Y., Machado, L., Popov, P., 2012. Constitutive model for the numerical analysis of phase transformation in polycrystalline shape memory alloys. Int. J. Plast. 32–33, 155–183. doi:10.1016/j.ijplas.2011.10.009.

Lagoudas, D.C., 2008. Shape memory alloys: Modeling and engineering applications. Springer US doi:10.1007/978-0-387-47685-8.

Leo, P.H., Shield, T.W., Bruno, O.P., 1993. Transient heat transfer effects on the pseudoelastic behavior of shape-memory wires. Acta Metall. Mater. 41 (8), 2477–2485. doi:10.1016/0956-7151(93)90328-P.

Liang, C., Rogers, C.A., 1990. One-dimensional thermomechanical constitutive relations for shape memory materials. J. Intell. Mater. Syst. Struct. 1 (2), 207–234. doi:10.1177/1045389X9000100205.

[1] For numerical implementation of the coupled model, readers are referred to MATLAB scripts shared on Github website via the link: https://github.com/mzzhuo/coupledModel-NiTi-SMA

Lim, T.J., McDowell, D.L., 2002. Cyclic thermomechanical behavior of a polycrystalline pseudoelastic shape memory alloy. J. Mech. Phys. Solids 50 (3), 651–676. doi:10.1016/S0022-5096(01)00088-6.

Matsuzaki, Y., Naito, H., 2004. Macroscopic and microscopic constitutive models of shape memory alloys based on phase interaction energy function: A Review. J. Intell. Mater. Syst. Struct. 15 (2), 141–155. doi:10.1177/1045389X04039953.

Mirzaeifar, R., DesRoches, R., Yavari, A., 2011. Analysis of the rate-dependent coupled thermo-mechanical response of shape memory alloy bars and wires in tension. Continuum Mech. Thermodyn. 23, 363–385. doi:10.1007/s00161-011-0187-8.

Morin, C., Moumni, Z., Zaki, W., 2011. A constitutive model for shape memory alloys accounting for thermomechanical coupling. Int. J. Plast. 27 (5), 748–767. doi:10.1016/j.ijplas.2010.09.005.

Morin, C., Moumni, Z., Zaki, W., 2011. Thermomechanical coupling in shape memory alloys under cyclic loadings: Experimental analysis and constitutive modeling. Int. J. Plast. 27 (12), 1959–1980. doi:10.1016/j.ijplas.2011.05.005.

Moumni, Z., Zaki, W., Nguyen, Q.S., 2008. Theoretical and numerical modeling of solidsolid phase change: Application to the description of the thermomechanical behavior of shape memory alloys. Int. J. Plast. 24 (4), 614–645. doi:10.1016/j.ijplas.2007.07.007.

Ortíin, J., Planes, A., 1989. Thermodynamics of thermoelastic martensitic transformations. Acta Metall. 37 (5), 1433–1441. doi:10.1016/0001-6160(89)90175-2.

Schweizer, B., Wauer, J., 2001. Atomistic explanation of the gough-Joule-effect. Eur. Phys. J. B 23, 383–390. doi:10.1007/s100510170058.

Shaw, J.A., 2000. Simulations of localized thermo-mechanical behavior in a NiTi shape memory alloy. Int. J. Plast. 16 (5), 541–562. doi:10.1016/S0749-6419(99)00075-3.

Shaw, J.A., Churchill, C.B., Iadicola, M.A., 2008. Tips and tricks for characterizing shape memory alloy wire: Part 1—differential scanning calorimetry and basic phenomena. Exp. Tech. 32 (5), 55–62. doi:10.1111/j.1747-1567.2008.00410.x.

Shaw, J.A., Kyriakides, S., 1995. Thermomechanical aspects of NiTi. J. Mech. Phys. Solids 43 (8), 1243–1281. doi:10.1016/0022-5096(95)00024-D.

Shaw, J.A., Kyriakides, S., 1997. On the nucleation and propagation of phase transformation fronts in a NiTi alloy. Acta Mater. 45 (2), 683–700. doi:10.1016/S1359-6454(96)00189-9.

Simo, J.C., Hughes, T.J.R., 1998. Computational inelasticity, 7. Springer-Verlag New York doi:10.1007/b98904.

Sun, Q., Zhao, H., Zhou, R., Saletti, D., Yin, H., 2012. Recent advances in spatiotemporal evolution of thermomechanical fields during the solidsolid phase transition. Comptes Rendus Mécanique 340 (4), 349–358. doi:10.1016/j.crme.2012.02.017.

Sun, Q.-P., Li, Z.-Q., 2002. Phase transformation in superelastic NiTi polycrystalline micro-tubes under tension and torsion—from localization to homogeneous deformation. Int. J. Solids Struct. 39 (13), 3797–3809. doi:10.1016/S0020-7683(02)00182-8.

Yin, H., 2013. Oscillations of thermal and mechanical fields during cyclic phase transition. Hong Kong University of Science and Technology.

Yin, H., He, Y., Sun, Q., 2014. Effect of deformation frequency on temperature and stress oscillations in cyclic phase transition of NiTi shape memory alloy. J. Mech. Phys. Solids 67, 100–128. doi:10.1016/j.jmps.2014.01.013.

Yin, H., Yan, Y., Huo, Y., Sun, Q., 2013. Rate dependent damping of single crystal CuAlNi shape memory alloy. Mater. Lett. 109, 287–290. doi:10.1016/j.matlet.2013.07.062.

Yu, C., Kang, G., Kan, Q., 2014. Study on the rate-dependent cyclic deformation of super-elastic NiTi shape memory alloy based on a new crystal plasticity constitutive model. Int. J. Solids Struct. 51 (25–26), 4386–4405. doi:10.1016/j.ijsolstr.2014.09.006.

Yu, C., Kang, G., Kan, Q., Song, D., 2013. A micromechanical constitutive model based on crystal plasticity for thermo-mechanical cyclic deformation of NiTi shape memory alloys. Int. J. Plast. 44, 161–191. doi:10.1016/j.ijplas.2013.01.001.

Yu, C., Kang, G., Kan, Q., Zhu, Y., 2015. Rate-dependent cyclic deformation of superelastic NiTi shape memory alloy: Thermo-mechanical coupled and physical mechanism-based constitutive model. Int. J. Plast. 72, 60–90. doi:10.1016/j.ijplas.2015.05.011.

Zaki, W., Moumni, Z., 2007. A 3D model of the cyclic thermomechanical behavior of shape memory alloys. J. Mech. Phys. Solids 55 (11), 2427–2454. doi:10.1016/j.jmps.2007.03.011.

Zaki, W., Moumni, Z., 2007. A three-dimensional model of the thermomechanical behavior of shape memory alloys. J. Mech. Phys. Solids 55 (11), 2455–2490. doi:10.1016/j.jmps.2007.03.012.

Zhang, X., Feng, P., He, Y., Yu, T., Sun, Q., 2010. Experimental study on rate dependence of macroscopic domain and stress hysteresis in NiTi shape memory alloy strips. Int. J. Mech. Sci. 52 (12), 1660–1670. doi:10.1016/j.ijmecsci.2010.08.007.

Zhuo, M., Xia, M., Sun, Q., 2019. Analytical solution of a mass-spring system containing shape memory alloys: Effects of nonlinearity and hysteresis. Int. J. Solids Struct. 171, 189–200. doi:10.1016/j.ijsolstr.2019.04.004.